nature communications

Article

https://doi.org/10.1038/s41467-025-57839-x

A supramolecular bactericidal material for preventing and treating plant-associated biofilms

Received: 8 June 2024

Accepted: 5 March 2025

Published online: 17 March 2025

Check for updates

Jinghan Yang[1,4], Kongjun Liu[1,2,4], Yazhen Chen[1], Haojie Ye[1], Gefei Hao[1], Fengpei Du[3] ✉ & Peiyi Wang[1] ✉

Treating bacterial biofilms on plants poses challenges due to biofilm induced resistance and poor agent adhesion on plant leaves. Here, we report on a host-guest self-assembled material which is biocompatible, has a lamellar supramolecular structure for leaf retention and prevents and treats bacterial biofilms. Phosphate/isopropanolamine-modified ferrocene forms a host-guest complex with β-CD which assembles into a lamella structure. The agent shows control efficacy against bacterial blight, bacterial leaf streak, and citrus canker in testing.

Bacterial biofilms pose a considerable agricultural challenge by shielding bacteria from plant immune defenses and bactericides[1–3]. It is recognized that bacterial biofilm infections are the primary culprits behind annual crop yield reductions ranging from 20% to 40%, with impact on major crops like rice[4–7]. Hence, there arises an urgent imperative to engineer bactericides proficient at impeding biofilm formation and/or dismantling established biofilms while effectively eliminating the enclosed bacteria[8,9]. Recently, biofilm inhibitors have been relatively well-documented in agricultural and medical contexts[10], yet biofilm eradicators remain seldom explored, with investigations primarily confined to animal models. Examples of such eradication agents include halogenated quinolines[11], bromophenazine derivatives[12], quaternary ammonium-functionalized biphen[n]arenes[13], and guanidinium-functionalized pillar[5]arenes[14]. Nevertheless, to the best of our knowledge, no documented bactericides capable of effectively eradicating biofilms in agricultural setting have yet emerged in the literature.

An impediment to biofilm eradication lies in the inefficient diffusion and absorption of active ingredients on leaf surfaces[15,16]. The intricate microstructure and distinct morphology of plant leaves, which serve as the primary contact portion for biocide droplets, affect their attachment and dispersion, limiting the effectiveness of bactericides[17–19]. For instance, the presence of trichomes, small papillae, and waxy coatings on rice leaf surfaces imparts superhydrophobic profiles that cause bactericide droplets to bounce, splash, and roll off, preventing effective coverage[20–22]. Recent efforts to improve pesticide deposition have focused on formulating active ingredients into various forms[23], such as nano emulsions[24], microcapsule suspensions[25–27], microemulsions[28], and water dispersible granules[29,30]. Although such formulations reduce active ingredient loss and improve deposition to some extent, they suffer from drawbacks including high costs, complex procedures, unclear auxiliary components, and insufficient bioavailability. Additionally, during crop protection efforts, organic solvents and surfactants have the potential to infiltrate water, soil, and air, leading to environmental issues like prolonged soil degradation and hazardous compound accumulation[31]. Thus, there is a pressing need for innovative strategies capable of facilitating the diffusion and absorption of bactericides to improve biofilm eradication and address the limitations of current formulations[32].

The emergence of supramolecular chemistry heralds great promise for pioneering effective strategies[33–35]. Not only do supramolecular-based bactericides bypass the formulation processes of traditional agents, but they also mitigate the ecological threats associated with the widespread use of surfactants and additives. Consequently, the crafted supramolecular bactericides imbue themselves with inherent environmental sustainability and ecological compatibility[36,37]. At the heart of supramolecular chemistry studies are interactions between hosts and guests, which lead to the creation of

[1]State Key Laboratory of Green Pesticide, Key Laboratory of Green Pesticide and Agricultural Bioengineering, Ministry of Education, Center for Research and Development of Fine Chemicals of Guizhou University, Guiyang, China. [2]Key Laboratory of Basic Pharmacology of Ministry of Education and Joint International Research Laboratory of Ethnomedicine of Ministry of Education, Zunyi Medical University, Zunyi, China. [3]Department of Applied Chemistry, College of Science, China Agricultural University, Beijing, China. [4]These authors contributed equally: Jinghan Yang, Kongjun Liu. ✉e-mail: dufp@cau.edu.cn; pywang@gzu.edu.cn

supramolecular structures made up of macrocyclic hosts and their guest molecules[38–41]. Among the common macrocyclic hosts molecules, including cyclodextrins (CDs), cucurbiturils (CBs), calixarenes (CAs), and crown ethers (CEs), cyclodextrins are particularly notable for being cost-effective and environmentally friendly cyclic oligosaccharides. Their central hydrophobic cavity enables spontaneous encapsulation of various active ingredients via specific complexation[42–46]. Ferrocene and its derivatives, recognized as exemplary guest molecules, have drawn considerable attention for their diverse pharmacological profiles[47], including antibacterial[48–50], antiviral[51], anti-tuberculosis[52], anticancer[53–55], and antioxidant[56] activities. Moreover, phosphate and isopropanolamine derivatives have been examined as bactericides, with both moieties identified as pivotal components for biofilm interventions[57]. It is proposed that linking phosphate and isopropanolamine with ferrocene may promote congruent antibacterial effects, specifically targeting biofilms. Meanwhile, the incorporation of ferrocene facilitates interaction with cyclodextrins, thus leveraging the multifaceted benefits of supramolecular chemistry, and potentially achieving dual actions of biofilm intervention and improved bioavailability.

In this work, we utilized an innovative supramolecular host-guest approach to enhance the physicochemical and biological properties of bioactive substrates, leading to the development of a superior supramolecular antibacterial material, FcP_{15}@β-CD. This material integrates the host molecule β-CD with a guest molecule phosphate/isopropanolamine-modified ferrocene (FcP_{15}) (Fig. 1). Driven by host-guest recognition, hydrogen bonding, and hydrophilic/hydrophobic interactions, FcP_{15}@β-CD exhibits balanced physicochemical properties and superior biocompatibility on plant leaves. Additionally, it effectively inhibits and eradicates biofilms, as evidenced by crystal violet staining, laser confocal scanning microscopy, and down-regulation of biofilm-related genes. Further antibacterial testing confirms its superior efficacy against bacterial leaf blight (BLB), bacterial leaf streak (BLS), and citrus bacterial canker (CBC), surpassing the performance of commercial thiodiazole-copper (TC) and FcP_{15}. In short, FcP_{15}@β-CD, leveraging host-guest interactions, offers enhanced control over bacterial disease by targeting biofilms, presenting promising prospects for plant bacterial disease prevention and management.

Results and discussion

Identification of preferred guest molecule FcP_{15}

Considering the preference of agriculture for agrochemicals characterized by simplicity, high bioactivity, and affordability, 20 small molecules, labeled FcP_1-FcP_{20} (Fig. 2 and Supplementary Figs. 43–127), were crafted by intentionally integrating phenyl cyclic-linked phosphates and isopropanolamines at a specific substitution of ferrocene scaffold, employing a concise synthesis procedure to identify potential guest molecules with high in vitro potency. The classical turbidimetric assay was employed to evaluate the in vitro potency of compounds FcP_1-FcP_{20} against the destructive bacterium *Xanthomonas oryzae* pv. *oryzae* (*Xoo*), with commercially available TC serving as a positive control[58]. As depicted in Table 1, the antibacterial potency was unsatisfactory when either fatty chains (FcP_{19} and FcP_{20}) or five-membered heterocycles (FcP_{17} and FcP_{18}) were introduced, prompting a shift from undesirable non-aromatic substituents to phenyl rings. However, unmodified phenyl rings performed poorly, and substitutions at inappropriate positions on the phenyl ring, such as the *ortho* and *meta* positions, impaired potency. In contrast, *para* substitutions proved beneficial, as evidenced by compounds FcP_6 (4-CF_3, EC_{50} = 9.16 μg/mL), FcP_8 (4-Cl, EC_{50} = 7.94 μg/mL), and FcP_{12} (4-OCH_3, EC_{50} = 6.79 μg/mL), which exhibited enhanced potency compared to their analogs with non-*para* substitutions, thereby distinguishing themselves. Given the consistent potency across these three compounds, deliberate optimization programs based on compound FcP_{12} were carried out. Incorporation of multiple substituents on the benzene ring decreased the anti-*Xoo* activity by comparing to those of compounds FcP_{13} (2,4-diOCH_3, EC_{50} = 16.03 μg/mL) and FcP_{14}

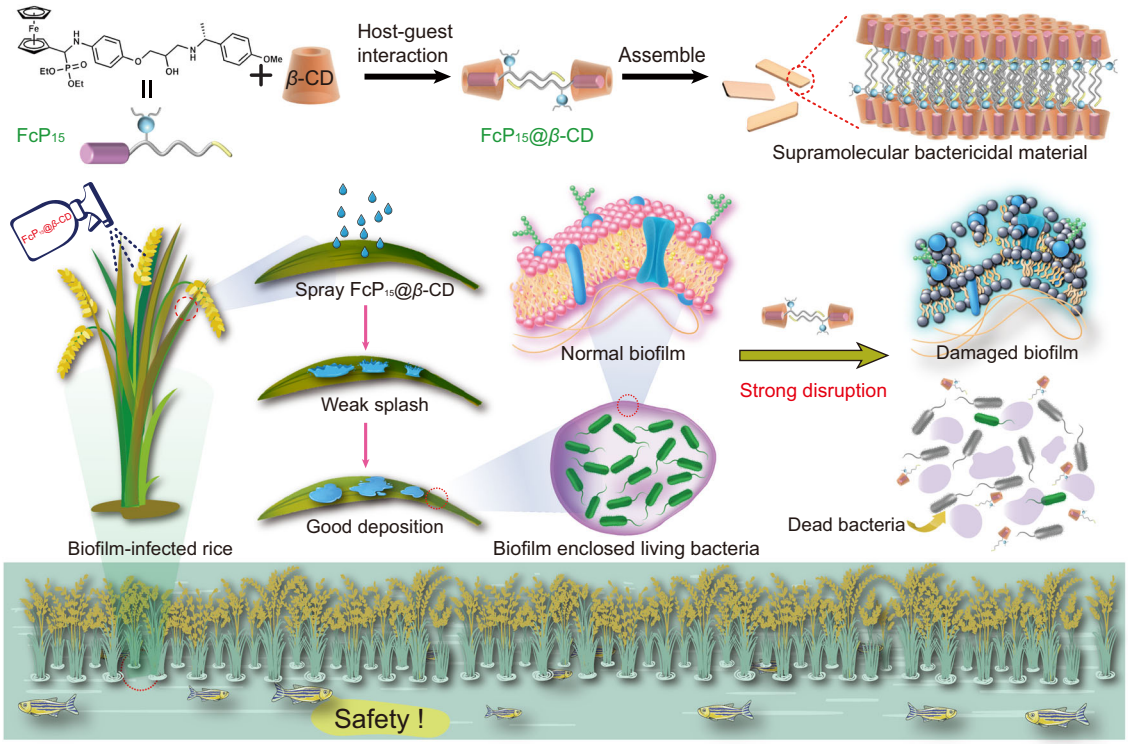

Fig. 1 | Preparation of supramolecular bactericidal materials for plant biofilm infection management. Schematic depiction of the preparation of potent functional supramolecular bactericidal materials with superior bioavailability for the management of plant biofilm infections.

https://doi.org/10.1038/s41467-025-57839-x

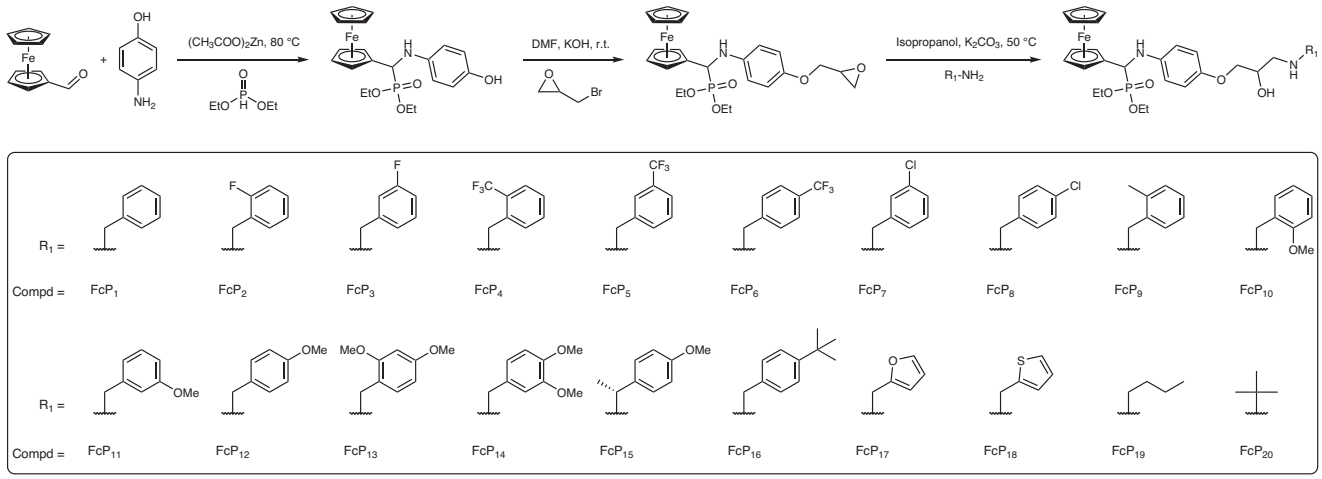

Fig. 2 | Design of target compounds with various substituents. General synthetic procedure for target molecules FcP_1-FcP_{20}.

Table 1 | Antibacterial efficacy of FcP_1-FcP_{20} compounds against *Xoo* in vitro

Compd	Inhibition ratio (%)		Regression equation	R^2	EC_{50}[a] (μg/mL)
	100 μg/mL	50 μg/mL			
Fc-CHO	55.25 ± 0.6	46.01 ± 1.2	$y = 1.154x + 2.863$	0.965	71.16 ± 0.10
1	57.21 ± 1.5	35.06 ± 0.6	$y = 1.610x + 1.942$	0.994	79.32 ± 3.05
2	49.76 ± 0.5	43.18 ± 2.2	$y = 1.230x + 2.602$	0.908	89.02 ± 4.32
FcP_2	98.1 ± 0.2	87.6 ± 0.6	$y = 1.861x + 2.298$	0.994	28.31 ± 0.76
FcP_3	100	100	$y = 3.746x + 0.822$	0.999	13.05 ± 0.03
FcP_4	97.1 ± 0.5	96.7 ± 0.6	$y = 4.561x - 0.052$	0.987	12.81 ± 0.06
FcP_5	100	100	$y = 2.679x + 1.965$	0.998	13.57 ± 0.45
FcP_6	98.1 ± 0.2	97.4 ± 0.2	$y = 1.575x + 3.485$	0.996	9.16 ± 0.02
FcP_7	100	86.3 ± 0.6	$y = 2.820x + 1.339$	0.984	19.67 ± 0.07
FcP_8	100	100	$y = 1.055x + 4.051$	0.995	7.94 ± 0.07
FcP_9	98.4 ± 0.3	97.8 ± 0.2	$y = 5.529x - 2.606$	0.982	23.75 ± 0.03
FcP_{10}	100	62.2 ± 0.3	$y = 1.445x + 2.688$	0.996	39.83 ± 0.50
FcP_{11}	98.1 ± 0.3	97.8 ± 0.1	$y = 5.451x - 2.141$	0.925	20.42 ± 0.04
FcP_{12}	100	100	$y = 1.024x + 4.148$	0.985	6.79 ± 0.03
FcP_{13}	98.1 ± 0.3	97.5 ± 0.3	$y = 4.383x - 0.281$	0.930	16.03 ± 0.10
FcP_{14}	100	77.3 ± 0.1	$y = 0.597x + 4.381$	0.985	10.89 ± 0.09
FcP_{15}	100	100	$y = 1.231x + 4.201$	0.960	4.45 ± 0.04
FcP_{15}@β-CD	100	100	$y = 1.239x + 4.262$	0.996	3.94 ± 0.08
FcP_{16}	100	100	$y = 0.966x + 4.230$	0.975	6.27 ± 0.09
FcP_{17}	100	89.7 ± 0.2	$y = 1.846x + 3.127$	0.993	10.35 ± 0.10
FcP_{18}	100	32.2 ± 0.4			>50
FcP_{19}	100	58.2 ± 0.1	$y = 1.578x + 2.481$	0.959	39.48 ± 0.50
FcP_{20}	100	100	$y = 0.976x + 4.057$	0.999	9.21 ± 0.08
TC[b]	62.3 ± 0.4	27.9 ± 0.7	$y = 3.620x - 1.772$	0.985	74.25 ± 0.45

Source data are provided as a Source Data file.
[a]The EC_{50} values, reflecting antibacterial effectiveness, are shown as the mean ± standard deviation.
[b]The commercial bactericide was used as the positive control, abbreviated as TC, which stands for thiodiazole copper.

(3,4-diOCH_3, EC_{50} = 10.89 μg/mL). Intriguingly, the introduction of an *S*-configured methyl at the α-position of *para*-methoxybenzyl group led to the creation of compound FcP_{15}. This compound demonstrated the highest activity within the series, with an EC_{50} value (4.45 μg/mL) merely 1/17th that of TC (EC_{50} = 74.25 μg/mL), 1/16th that of Fc-CHO (EC_{50} = 71.16 μg/mL), 1/18th that of intermediate 1 (EC_{50} = 79.32 μg/mL), and 1/20th that of intermediate 2 (EC_{50} = 89.02 μg/mL). Encouraged by this potency, FcP_{15} has been identified as the prime candidate for crafting supramolecular materials, paving the way for detailed investigations into driving forces, assembly behaviors, deposition profiles, antibacterial mechanisms, and in vivo efficacy.

Preparing methods, driving forces, assembly process, and stability studies of host–guest supramolecular material FcP_{15}@β-CD

To synthesize the FcP_{15}@β-CD host-guest complex, we used a simple and efficient method. Specifically, the guest molecule FcP_{15} (4.0 μL, 76.8 mM) in a tetrahydrofuran (THF) solution was added dropwise into

https://doi.org/10.1038/s41467-025-57839-x

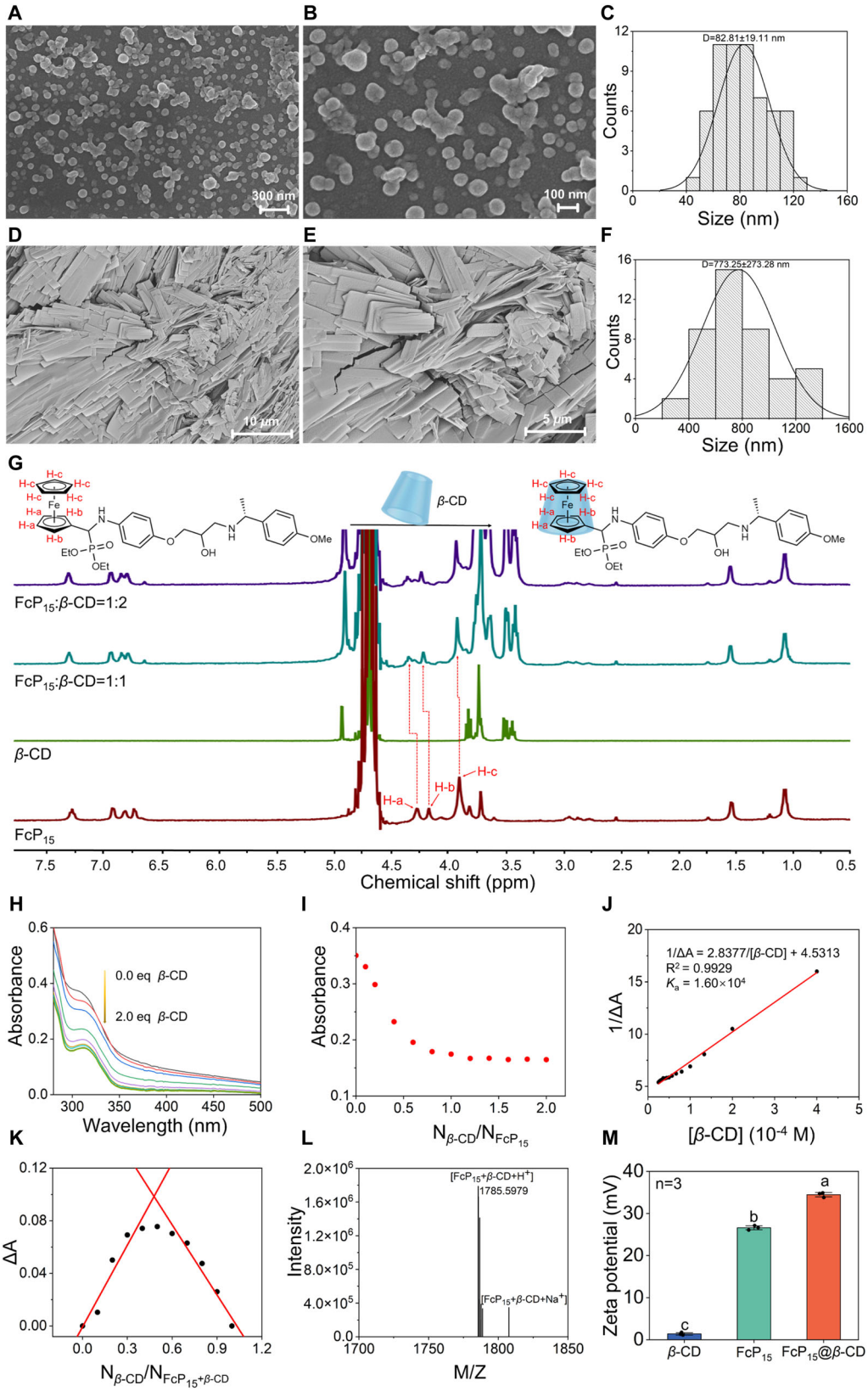

1.0 mL of deionized water solution containing the host molecule β-CD (0.31 mM). The natural evaporation of THF resulted in the formation of self-assembled supramolecular structures, which were extensively characterized in terms of topological microstructure, driving forces, binding stoichiometry, and system stability using scanning electron microscopy (SEM), ^{1}H NMR titrimetry, UV–visible titrimetry, high-resolution mass spectrometry (HRMS), Zeta potential and high-performance liquid chromatography (HPLC).

Firstly, SEM was used to observe the morphology of both the guest molecule and supramolecule. As depicted in Fig. 3A–F, FcP_{15} exhibited a spherical morphology with particle sizes ranging from 40 to 120 nm, whereas, upon encapsulation by one equivalent of β-CD, the

Fig. 3 | Characterization of FcP_{15}@β-CD. A, **B** SEM images of FcP_{15}. **C** Size distributions of FcP_{15}. **D**, **E** SEM images of FcP_{15}@β-CD. **F** Size distributions of FcP_{15}@β-CD. **G** ^{1}H NMR spectra of FcP_{15}, β-CD, and mixtures of FcP_{15} and β-CD at molar proportions of 1:1 and 1:2 in D_2O, with a FcP_{15} concentration of 5.0 mM. **H** UV–vis titration curves for FcP_{15} (0.1 mM) in the presence of increasing molar equivalents of β-CD (0–2.0 eq). **I** Linearity of absorption spectra at 315 nm of FcP_{15} with respect to β-CD at various concentrations. **J** Benesi–Hildebrand plots of 1/ΔA versus 1/β-CD. **K** Job's method of continuous plot of ΔA at 315 nm, with FcP_{15} and β-CD concentrations both set to 0.1 mM in H_2O. **L** High-resolution mass spectrum of FcP_{15}@β-CD. **M** Measurement of Zeta potential of FcP_{15}@β-CD, FcP_{15}, and β-CD in aqueous solution. In (**M**), the error bars show the mean ± standard error (SE). Statistically significant differences were assessed using one-way ANOVA followed by the least significant difference (LSD) post-hoc test, with different letters indicating significant variations ($n = 3$, $p < 0.05$). The experiments were performed with at least three replicates. Source data are provided as a Source Data file.

supramolecule showcased distinct morphological characteristics, featuring a rectangular surface morphology and an average width of 773 nm, representing a highly intuitive outcome of supramolecular assembly.

The driving forces behind self-assembly were investigated through the following studies. Regarding the ^{1}H NMR titration experiments in D_2O (Fig. 3G and Supplementary Table 1), the chemical shifts of the three sets of protons on the ferrocene moiety were recorded at 4.24 ppm (H-a), 4.14 ppm (H-b), and 3.88 ppm (H-c), respectively. When 1.0 equivalent of β-CD was added, all proton signals (H-a, H-b, and H-c) experienced downfield shifts, with corresponding chemical shift changes of +0.08, +0.05, and +0.02 ppm ($\Delta\delta$), respectively. The manifestation of peak shifts observed in ^{1}H NMR titration experiments align with that documented in β-CD encapsulation behavior[59–61], robustly indicating the deep-seated encapsulation of the ferrocene moiety within the β-CD cavity. Nevertheless, despite the consecutive addition of 2.0 equivalents of β-CD, the chemical shifts of the protons (H-a, H-b, H-c) remained unchanged, indicating a one-to-one association between the host and the guest. To track the fluctuation in absorption peak intensities during supramolecule formation, varying concentrations of β-CD were incrementally added to a 0.1 mM FcP_{15} solution for UV-visible titration. The absorption at 315 nm consistently decreased with the addition of β-CD until an equivalent concentration was reached, beyond which minimal change in absorption occurred (Fig. 3H–J). This behavior mirrors the β-CD encapsulation dynamics documented in the literature, reaffirming the 1:1 binding ratio between the host and guest. Meanwhile, the titration experiments produced the Eq. $1/\Delta A = 2.8377/[\beta\text{-CD}] + 4.5313$, with a binding constant of $1.60 \times 10^4\ M^{-1}$ (Fig. 3J), suggesting the relatively stable nature of the host-guest binding[62,63]. Additionally, the concentration-dependent UV/Vis spectroscopy was performed to elucidate the self-assembly. As shown in Supplementary Fig. 1A, increasing the concentration of FcP_{15}@β-CD led to an expansion of the absorption band from 350 to 600 nm, indicating the formation of a large number of nanoparticles, which contributes to the increase in system turbidity. However, this phenomenon was quickly disrupted by gradually introducing a proportion of methanol (CH_3OH), a strong hydrogen bonding disruptor, confirming that the hydrogen bonding force is an important driving force (Supplementary Fig. 1B). Various composite patterns, each with different FcP_{15}/β-CD ratios, were presented to elucidate the process of the nanosphere-to-nanosheet transformation (Supplementary Fig. 2). Clearly, upon adding 0.1 equivalent of β-CD, large spherical aggregates became apparent. This suggests that the specific loading of FcP_{15} into the cavity of β-CD led to the disassembly of original nanospheres and the rearrangement of the building block FcP_{15}@β-CD. By progressively increasing the amount of β-CD to 0.2 or 0.4 equivalents, a significant formation of snowflake-like thin films was observed, implying the involvement of additional host-guest units in the reassembly. Remarkably, when the proportion of FcP_{15} to β-CD was 1:0.6 or 1:0.8 (molar ratio), irregular lamellar structures were formed. Additionally, since FcP_{15} binds to β-CD at a 1:1 ratio, the excess β-CD at a 1:1.2 ratio cannot self-assemble, and the structure of these lamellae does not appear to be drastically altered.

The 1:1 complexation ratio between FcP_{15} and β-CD was confirmed through Job's plots and HRMS analysis. As illustrated in Fig. 3K, L, once the molar fraction of β-CD reached 0.5, ΔA peaked, while a molecular weight of 1785.5979 was observed in HRMS, precisely matching the theoretical molecular weight of [FcP_{15} + β-CD + H^+]. Additionally, FcP_{15}@β-CD exhibited a Zeta potential of 34.46 mV (Fig. 3M), notably higher than FcP_{15} (26.61 mV), indicating that the formation of host-guest complexes contributes to enhancing solution stability.

Given the above investigations, we speculated a possible mechanism for lamellar assembly (Fig. 1). Initially, a binary building block, FcP_{15}@β-CD, was constructed based on host-guest recognition principle between β-CD and the ferrocene moiety of FcP_{15}. Then, these building units stagger to evade exposure of hydrophobic groups to the aqueous environment, subsequently assembling into a layered thin-film structure. Finally, leveraging hydrogen bonding interactions, all the layered structures combined themselves together to form lamellar architectures. For the self-assembly of FcP_{15}, a possible mechanism was proposed. Considering the amphiphilic nature of FcP_{15}, the hydrophilic isopropanolamine part would come into contact with the aqueous environment via hydrogen bonding, while the hydrophobic phosphate/ferrocene part remains concealed inside (Supplementary Fig. 3C). Thus, with the synergistic assistance of hydrogen bonding and hydrophilic/hydrophobic interactions, the amphiphile FcP_{15} tends to assemble into spherical structures. The mentioned driving force was confirmed by concentration-dependent and methanol-disruptive experiments on FcP_{15} (Supplementary Fig. 3A, B). Finally, to assess the stability of the supramolecular system, Zeta potential and HPLC measurements were conducted under varying storage durations, temperatures, and pH conditions. As displayed in Supplementary Figs. 4–10, after 7 days of storage, the supramolecular complex (FcP_{15}@β-CD) showed relatively lower degradation rates within 1.84–3.74% and 0.00–6.39%, respectively. In contrast, the FcP_{15} itself gave large degradation rates of 4.22–9.16% and 3.73–9.55%, respectively. This outcome indicates that optimizing FcP_{15} by β-CD via the flexible supramolecular technique can enhance the stability of bioactive ingredients in a water environment. This inference was further verified by Zeta potential measurements (Supplementary Fig. 11). After storing for 7 days, the Zeta potential of FcP_{15}@β-CD system changed from 34.46 to 33.74 mV, a decrease of 2.1%, while that of FcP_{15} system had a variation from 26.61 to 21.74 mV, a decrease of 18.3%. In a word, a stable and biocompatible supramolecular complex system was successfully fabricated by rationally manipulating the host-guest supramolecular strategy, which holds the potential to enhance the bioavailability of bioactive substrates.

Enhanced deposition performance of FcP_{15}@β-CD on rice leaf surface

Efficient deposition is of paramount importance in facilitating the nuanced interaction between pharmaceuticals and foliar targets[64]. Nonetheless, inherent limitations of conventional pesticides often result in the inadequate persistence of drug droplets on leaf surfaces, thereby culminating in suboptimal pesticide efficacy and environmental contamination. We conducted a comprehensive assessment of the deposition attributes of FcP_{15} and FcP_{15}@β-CD on rice foliage, employing a battery of experiments encompassing solubility profiling, surface tension measurements, contact angle determination, droplet spraying dynamics, rebound kinetics, splashing behavior assessment,

https://doi.org/10.1038/s41467-025-57839-x

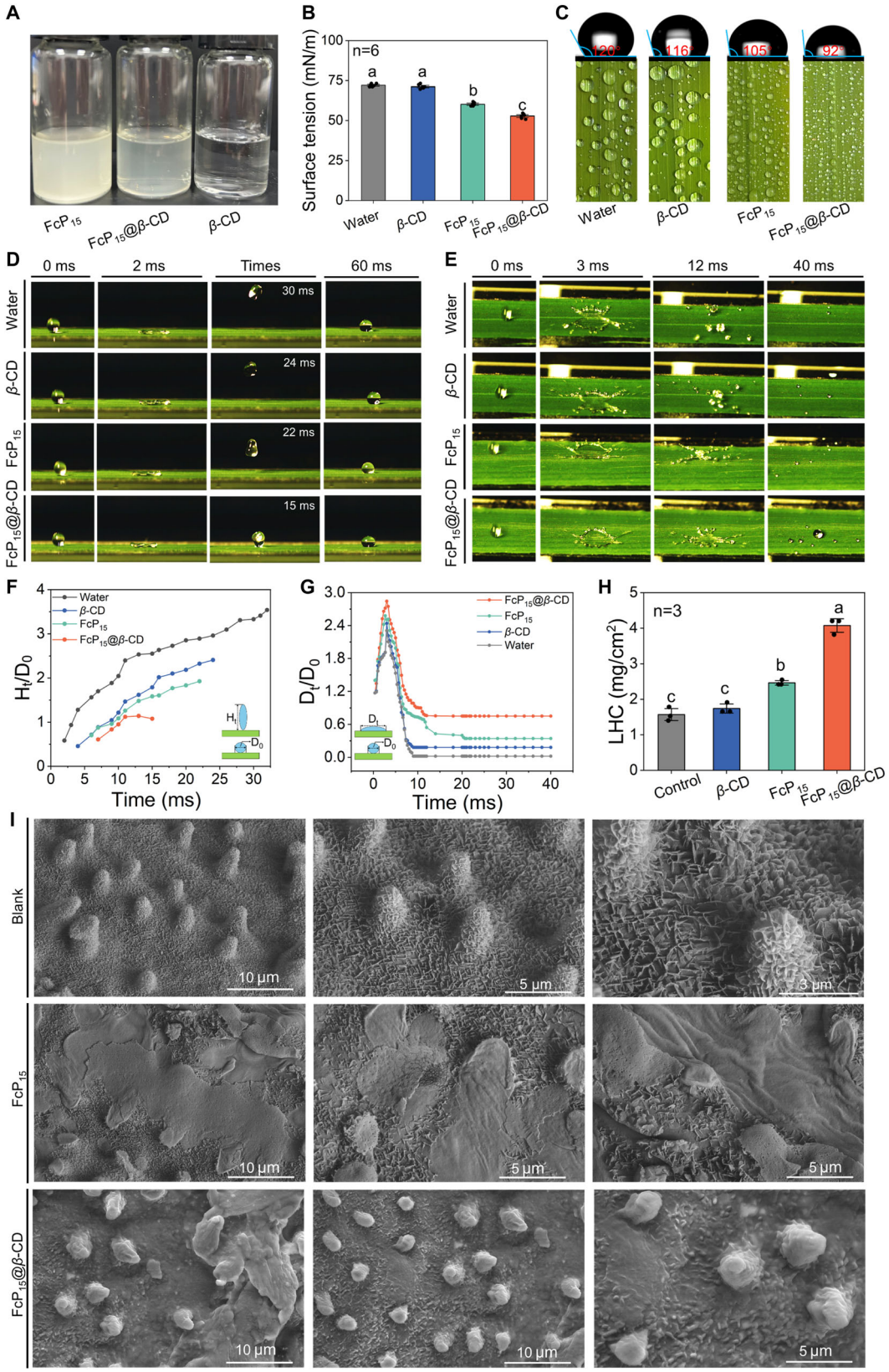

retention volume quantification, and SEM imaging. Our endeavor focused on revealing the advantages of freshly constructed supramolecular material in terms of its physicochemical profiles.

In terms of solubility, the solution of FcP_{15}@β-CD exhibited greater transparency compared to that of FcP_{15} alone at identical concentrations (Fig. 4A), implying enhanced solubility of the supramolecular material. This enhancement could be ascribed to the effective encapsulation of hydrophobic ferrocene moiety by the external hydrophilic β-CD, facilitating its interaction with surrounding water molecules. Concerning surface tension, excessive levels can cause droplet rebound and rolling during spraying, impeding effective deposition on plant leaves[65]. Fortunately, the supramolecular material

Fig. 4 | Physicochemical properties and foliar affinity of FcP_{15} and FcP_{15}@β-CD. **A** Images of aqueous solutions of FcP_{15}, FcP_{15}@β-CD, and β-CD. **B** Surface tension and **C** contact angle measurements for aqueous solutions of water, β-CD, FcP_{15}, and FcP_{15}@β-CD at 200 μg/mL. **D** Images depicting droplet rebound behavior on the rice surface, droplet dropped from 10 cm. **E** Images showing droplet splash behavior on the rice surface, droplet dropped from 35 cm. **F** Time-dependent changes in the normalized droplet touch diameter (H_t/D_0) for aqueous solutions including water, β-CD, FcP_{15}, and FcP_{15}@β-CD droplets during the droplet bounce test. **G** Time-dependent variations in the normalized touch diameter (D_t/D_0) for aqueous solutions including water, β-CD, FcP_{15}, and FcP_{15}@β-CD droplets during the droplet splash test. **H** Liquid holding capacities of rice leaves after immersion in different solutions. **I** Scanning electron microscopy images comparing untreated rice leaf, rice leaf treated with FcP_{15}, and rice leaf treated with FcP_{15}@β-CD. In (**B**, **H**), error bars show the mean ± standard error (SE). Different letters indicate statistically significant differences, as determined by one-way ANOVA and subsequent least significant difference (LSD) post-hoc test ($p < 0.05$). The experiments were carried out with a minimum of three replicates, and the sample size for each data point is provided in the respective figure. Source data are provided as a Source Data file.

we fabricated exhibited a lower surface tension of 52.75 mN/m compared to 60.24 mN/m for the individual guest molecule (Fig. 4B), indicating an enhancement in the deposition performance of the solution through supramolecule formation. As for contact angle, smaller values denote easier spreading and wetting on plant leaves[66]. The contact angle of FcP_{15}@β-CD on rice leaves decreased by 13° in comparison to that of FcP_{15} (Fig. 4C), indicating that FcP_{15}@β-CD exhibits greater propensity for spreading and wetting on rice leaves relative to the guest alone. To visually evaluate the effect of FcP_{15}@β-CD on leaf surface wetting, solutions containing β-CD/FcP_{15}/FcP_{15}@β-CD and water were sprayed on rice leaves to compare droplet sizes and density. Among them, droplets containing FcP_{15}@β-CD exhibited smaller size and higher density compared to the other groups (Fig. 4C), indicative of their superior wetting profiles.

The application of pesticides on rice leaves can induce splashing, rebounding, and mobility, compromising control efficiency[67]. Surprisingly, the supramolecular material we developed demonstrated superior mitigation of these occurrences. As depicted in Fig. 4D, F, alongside Supplementary Movie 1, high-speed cameras documented the droplet deposition process of the supramolecule and the two individual molecules on the leaves. Notably, water and β-CD solutions exhibited complete spherical rebounding with relatively high rebound heights. In contrast, the rebound height decreased slightly for FcP_{15}, with a further reduction observed for FcP_{15}@β-CD. To visualize the impact dynamics, we assessed the normalized rebound height over time (H_t/D_0), where H_t represents the distance between the rice leaf surface and the top of the droplet, and D_0 denotes the initial diameter of the droplet. Lower values of H_t/D_0 indicate better suppression of droplet rebound. As shown in Fig. 4F, the H_t/D_0 for water, β-CD, and FcP_{15} was 2.70, 2.08, and 1.58, respectively, substantially higher than those for droplets containing FcP_{15}@β-CD (0.84), highlighting the superior suppression of droplet rebound by FcP_{15}@β-CD. The splashing behavior of liquid droplets on rice leaves underwent examination. As shown in Fig. 4E, G, as well as in Supplementary Movie 2, the FcP_{15}@β-CD solution displayed a larger maximum impact area (at 3 ms) on rice leaves compared to the water, β-CD, and FcP_{15} solutions, with no splashing occurring.

Additionally, to better understand the impact dynamics, we examined their normalized droplet contact diameters throughout the period (D_t/D_0, D_t and D_0 refer to corresponding contact diameter and initial diameter of droplets). As presented in Fig. 4G, the maximum D_t/D_0 was achieved as 2.84 (FcP_{15}@β-CD) and 2.51 (FcP_{15}), suggesting that the combination of FcP_{15} and β-CD into a supramolecular structure effectively reduces droplet splashing. Subsequently, the adhesion of FcP_{15} and FcP_{15}@β-CD was assessed via the LHC, which explicitly signifies the deposition of active compounds on rice leaves[68]. The LHC value of the FcP_{15}@β-CD group increased compared to that of FcP_{15} (Fig. 4H), suggesting that the resulting supramolecular material adheres more readily to the surface of rice leaves. In the end, to observe the droplet structures on rice leaves, we used SEM to analyze the FcP_{15} and FcP_{15}@β-CD droplets. As depicted in Fig. 4I, untreated rice leaves displayed distinct waxy cuticles and trichomes. Furthermore, the FcP_{15}@β-CD solution effectively enveloped the waxy cuticles with a remarkably uniform distribution and coverage across the leaf surface compared to FcP_{15}. This outcome indicated that FcP_{15}@β-CD exhibited strong interactions and good biocompatibility with the leaf surface, facilitating the penetration and the agents settling and entering the leaves.

In brief, the findings indicate that the lamellar supramolecular material we developed possesses distinct physicochemical profiles compared to individual guest molecules, enabling their formulated solutions to efficiently deposit on superhydrophobic leaves and facilitate leaf wetting.

Dual actions of biofilm inhibition and eradication by FcP_{15}@β-CD through multiple pathways

Xoo stands as the principal Gram-negative pathogen accountable for biofilm-related infections[69]. Hence, we employed *Xoo* as the primary pathogen for a series of investigations, assessing the impact of the host, guest, and FcP_{15}@β-CD on *Xoo*-associated biofilms using crystal violet staining. The findings reveal that β-CD has no discernible impact on biofilm formation (Supplementary Fig. 12), whereas both FcP_{15} and FcP_{15}@β-CD exhibit detectable inhibition on *Xoo* biofilm formation (Fig. 5A–C). Within the tested concentration range, the inhibitory effect escalates with increasing concentration. FcP_{15} demonstrates a biofilm inhibition rate of 63.03%, while FcP_{15}@β-CD increases this rate to 74.73% at a lower concentration of 8.90 μg/mL ($2.0 \times EC_{50}$). Notably, at concentrations of $4.0 \times EC_{50}$ and $8.0 \times EC_{50}$, the anti-biofilm inhibition rate of the supramolecule rises to 89.28% and 94.85%, respectively, surpassing that of the individual guest molecules at corresponding concentrations. Of particular note is that the material exhibited minimal impact on bacterial growth while effectively inhibiting biofilm formation at concentrations below $2.0 \times EC_{50}$ (Supplementary Fig. 13). It was observed that *Xoo* cell growth was restricted at a concentration of $8.0 \times EC_{50}$, indicating that a high concentration of FcP_{15}@β-CD can both inhibit biofilm formation and suppress bacterial proliferation simultaneously. To further substantiate the material's inhibitory effect on bacterial growth, we administered FcP_{15} and FcP_{15}@β-CD to *Xoo* colonies following the cultivation of *Xoo* biofilms[70]. As depicted in Fig. 5D, E, FcP_{15}@β-CD notably diminished the bacterial colony count within *Xoo* biofilms, surpassing the inhibitory effect of the individual FcP_{15}. At $2.0 \times EC_{50}$, the FcP_{15}@β-CD treatment group exhibited a minimum colony forming units of 63×10^5 CFU/mL, merely 1/6 of the negative control, underscoring its considerable inhibitory effect on biofilm-protected bacterial growth. Given the pronounced inhibitory effects of FcP_{15} and FcP_{15}@β-CD on biofilm formation, coupled with the fact that planktonic bacteria constitute the majority of the bacterial population in the broth, whereas biofilm-enclosed bacteria represent only a small fraction, the number of planktonic bacterial colonies remains relatively unaffected at lower reagent concentrations. In contrast, a reduction in the number of *Xoo* within the biofilm is observed. To substantiate this hypothesis, both untreated bacteria (comprising planktonic and biofilm-enclosed bacteria) and biofilm-enclosed bacteria were cultured on solid NA medium. As illustrated in Supplementary Fig. 14, for untreated bacteria, exposure to FcP_{15} at $2.0 \times EC_{50}$ led to only a modest reduction in the number of viable *Xoo* colonies, relative to the control (0.4% DMSO and β-CD), indicating that only a minor fraction of the bacterial population was

https://doi.org/10.1038/s41467-025-57839-x

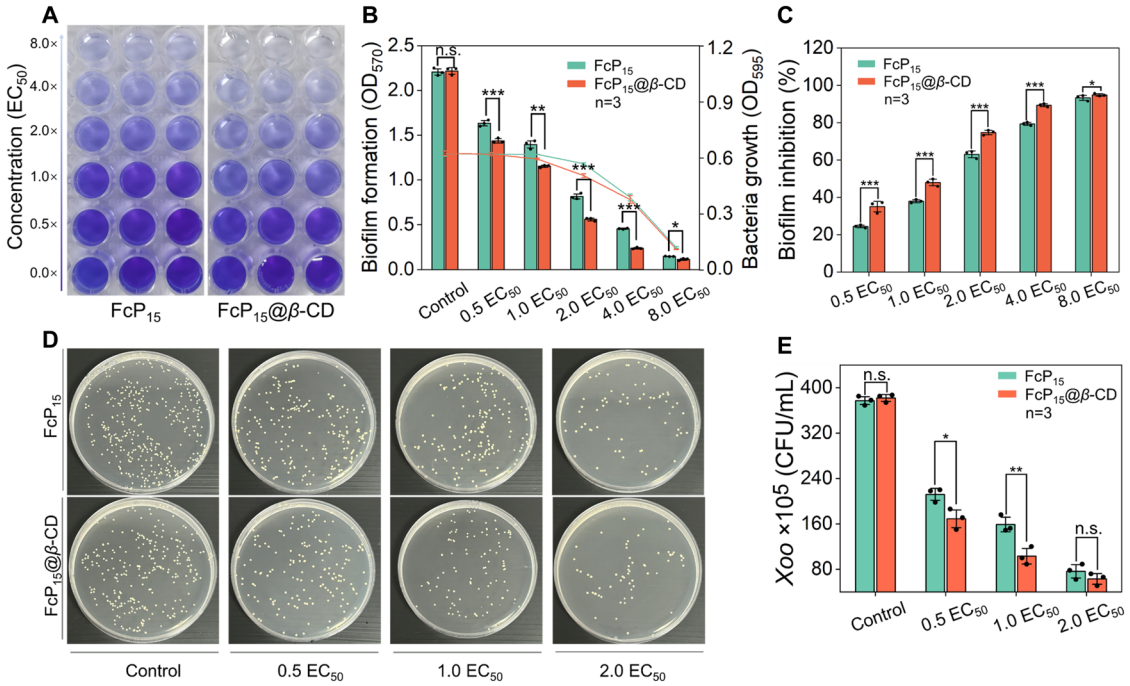

Fig. 5 | The inhibition of biofilm formation by FcP_{15} and FcP_{15}@β-CD. A Crystal violet staining analysis showing the effect of FcP_{15} and FcP_{15}@β-CD on *Xoo* biofilm formation (ranging from 0.5 × EC_{50} to 8.0 × EC_{50}) over 48 h. **B** The absorbance at 570 nm and 595 nm was measured to evaluate the remaining biofilm and the level of bacterial proliferation. **C** The biofilm inhibition rates were derived from the OD_{570} nm values after treatment with FcP_{15} and FcP_{15}@β-CD. **D** *Xoo* forms biofilm colonies after treatment with different concentrations of FcP_{15} and FcP_{15}@β-CD on NA solid medium. **E** Enumeration of *Xoo* colonies from the agar plates after treatment. For (**B**, **C**, **E**), error bars represent means ± standard error (SE), and statistically significant differences between the means were determined using Student's *t* test, with significance levels indicated as $^{*}p < 0.05$, $^{**}p < 0.01$, and $^{***}p < 0.001$; n.s. denotes no significance. The experiments were conducted with a minimum of three replicates, and the sample size for each data point is specified within the respective figure. Source data are provided as a Source Data file.

eliminated. However, a decrease in the number of biofilm-enclosed bacteria, relative to the control, was observed in Fig. 5D, where ~80% of the biofilm-enclosed bacteria were eradicated. This reduction in biofilm-enclosed bacteria was further corroborated by 3D CLSM imaging, as presented in Supplementary Fig. 15.

Besides its impact on inhibiting biofilm formation, we delved into exploring the supramolecular material's ability to eradicate biofilms. Initially, we examined the formation and progression of *Xoo* biofilms at various time points, revealing that biofilms tended to mature after 48 h of cultivation of *Xoo* (Supplementary Fig. 16). Subsequently, we assessed the eradication potential of FcP_{15} and FcP_{15}@β-CD on preformed bacterial biofilms. As illustrated in Fig. 6A, B, at a concentration of 2.0×EC_{50}, FcP_{15} and FcP_{15}@β-CD demonstrated biofilm disruption rates of 37.19% and 46.64%, respectively. In addition, the elimination effect was augmented with increasing concentration, with the disruption rate exceeding 80% for both treatment groups at a concentration of 16×EC_{50}. Meanwhile, the supramolecule exhibited more potent disruptive effects in comparison to the guest molecule alone (Fig. 6B). In parallel with the noted suppression of bacterial growth during biofilm eradication, the administration of FcP_{15} and FcP_{15}@β-CD likewise elicited a concentration-dependent decline in *Xoo* cell population, based on the achieved colony-forming units within established biofilms (Fig. 6C, D). Additionally, the inhibitory potency of FcP_{15} consistently lagged behind that of FcP_{15}@β-CD. After treatment with FcP_{15}@β-CD, the number of colonies decreased by 38.96%, 74.26%, and 84.53% at concentrations of 2.0×, 4.0× and 8.0 × EC_{50}, respectively, compared to the control, demonstrating significant inhibition. It can be inferred that damaging mature biofilms and biofilm-protected bacteria is more difficult and requires higher dosages. Fortunately, the performance of FcP_{15}@β-CD validates that the current fabricated material is a robust candidate for biofilm disruptors. This declaration was further validated by confocal laser scanning microscopy (CLSM) 3D imaging (Fig. 6E and Supplementary Fig. 17), in which live and deceased bacteria residing in the *Xoo* biofilm were stained employing a blend of acridine orange (AO) and propidium iodide (PI). Clearly, application of FcP_{15}@β-CD engendered a rise in the count of deceased *Xoo* cells within the biofilm, in tandem with escalating dosages, evincing increasingly intense red fluorescence. Conversely, numerous bacteria in the control cohort persisted in viability, displaying robust green fluorescence alongside weak red fluorescence. Moreover, based on the statistical average green and red fluorescence intensity (Fig. 6F, G), FcP_{15}@β-CD still exhibited superior annihilating ability compared to the single FcP_{15}, suggesting enhanced bioavailability. SEM images in Supplementary Fig. 18 were used to evaluate the damaging effects of FcP_{15}@β-CD on preformed biofilms of *Xoo*. Comparing to the control, where *Xoo* cells were well-embedded within a dense biofilm, FcP_{15}@β-CD treatments with different doses led to the reduced biofilm density and the exposure of bacteria outside, demonstrating effective eradication potency. In particular, at the dose of 8.0×EC_{50}, the related pre-established biofilms were almost completely disrupted and accompanied by the appearance of broken, wrinkled, and incomplete bacteria. These outcomes were consistent with CLSM 3D imaging, verifying that FcP_{15}@β-CD was capable of effectively damaging mature biofilms.

To illustrate the biofilm penetrability of FcP_{15}@β-CD, its entrance into pre-established biofilms was assessed by HPLC determination. As shown in Supplementary Figs. 19–20, compared with the sample without biofilms, the content of FcP_{15}@β-CD in the supernatant gradually decreased with the prolongation of the culture time in the presence of *Xoo* biofilms. This outcome indicates that FcP_{15}@β-CD is capable of entering bacterial biofilms. Besides this, SEM imaging and Energy Dispersive X-ray Spectroscopy (EDS) assessment were also utilized.

https://doi.org/10.1038/s41467-025-57839-x

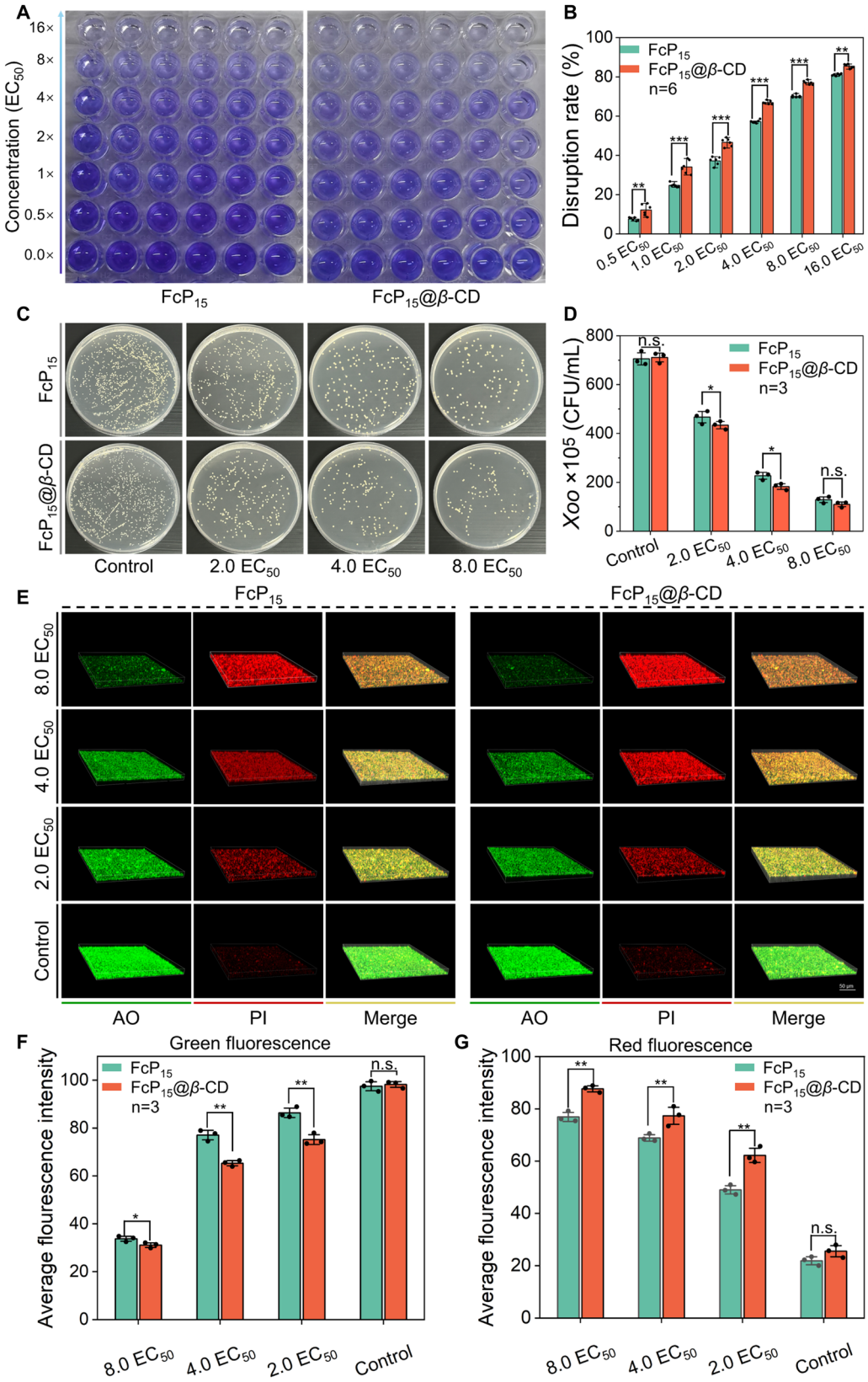

As presented in Supplementary Fig. 21, some lamellar assemblies were observed to coexist with bacteria. Further EDS analysis found that the FcP_{15}@β-CD treatment group contained a certain amount of iron (Fe), which was probably due to the ferrocene group of FcP_{15}@β-CD. In contrast, we did not detect iron (Fe) in the control group, which preliminarily reveals that the supramolecular complex has good permeability.

Potential bactericidal mechanisms of FcP_{15}@β-CD and its multifaceted functions

To investigate the bactericidal mechanism of FcP_{15}@β-CD, we first assessed bacterial electrolyte leakage and cell membrane permeability using a relative conductivity test[71]. As shown in Supplementary Fig. 22, co-incubation with varying concentrations of FcP_{15}@β-CD led to a

Fig. 6 | The eradication of mature biofilm by FcP_{15} and FcP_{15}@β-CD. A Images illustrating pre-established biofilms assessed using crystal violet staining. **B** Quantification of pre-established *Xoo* biofilm destruction following exposure to varying doses of FcP_{15} and FcP_{15}@β-CD. **C** Development of *Xoo* colonies within established biofilms on solid NA medium after exposure to various concentrations of FcP_{15} and FcP_{15}@β-CD. **D** Performing a quantitative assessment of *Xoo* colonies on the agar plates. **E** 3D CLSM images depicting *Xoo* communities in established biofilms following exposure to varying concentrations of FcP_{15} and FcP_{15}@β-CD. The biofilm cells were stained sequentially with AO (green: live cells) and PI (red: dead cells), with a scale bar of 50 μm. **F**, **G** Enumeration of live (Green fluorescence area) and deceased (red fluorescence area) *Xoo* communities from the aforementioned CLSM 3D images using Image-J. In (**B**, **D**, **F**, **G**), error bars represent the mean ± standard error (SE). Statistical analysis of the differences between means was carried out using Student's *t*-test, with significance levels indicated as $^{*}p < 0.05$, $^{**}p < 0.01$, and $^{***}p < 0.001$; n.s. denotes no significant difference. Each experiment was performed with at least three independent replicates, and the sample size for each data point is clearly indicated in the respective figure. Source data are provided as a Source Data file.

progressive increase in relative conductivity. Notably, at concentrations of $2\times EC_{50}$ and $4\times EC_{50}$, the conductivity values were higher compared to FcP_{15} under identical conditions. This outcome reveals that FcP_{15}@β-CD has better membrane permeability and consequently results in bacterial electrolyte leakage. On the other hand, excessive ROS (reactive oxygen species) accumulation in bacteria can disturb various physiological responses, causing redox imbalances and oxidative stress damage[72,73]. Thus, the ROS levels were monitored by a commercial ROS assay kit (Supplementary Fig. 23). As the dose of FcP_{15}@β-CD increased, the ROS levels rose in a dose-dependent manner, surpassing those observed with FcP_{15}. This indicates that FcP_{15}@β-CD treatment led to a greater accumulation of ROS. This finding was in agreement with the CLSM images in Supplementary Fig. 24. To gain deeper insights into the underlying mechanisms, the activities of catalase (CAT) and superoxide dismutase (SOD), enzymes that adjust excessive ROS levels, were measured in *Xoo* strains using the appropriate commercial kits. Notably, the activities of these two enzymes were inhibited after incubation with FcP_{15}@β-CD (Supplementary Fig. 25). Based on the above investigations, a potential mechanism for the bactericidal activity of FcP_{15}@β-CD has been suggested. The designed supramolecular material, FcP_{15}@β-CD, exhibits enhanced biocompatibility and can enhance membrane permeability while disrupting the bacterial redox system. This disruption leads to electrolyte leakage, physiological imbalance, oxidative stress, and ultimately, bacterial cell death.

To delve into the mechanism by which the supramolecule targets biofilms and exerts inhibitory and disruptive effects, we pursued further mechanistic inquiries. *Xoo* generates a distinct extracellular polysaccharide (EPS) governed by the *gum* gene cluster, essential not only for fortifying biofilm structure but also for their initiation, maintenance, and facilitating *Xoo* chemotaxis[74–76]. The frequently used weight method was employed to evaluate the impact of the guest molecule and the supramolecule on EPS production by *Xoo*. As depicted in Fig. 7A, both FcP_{15} and FcP_{15}@β-CD suppressed EPS production in a concentration-dependent fashion, with the supramolecule demonstrating superior inhibition compared to the individual guest molecule across all dosage levels. Notably, supramolecule treatment resulted in a 57.74% decrease in EPS content at the low concentration of $2.0\times EC_{50}$. To accurately measure EPS contents, a classical phenol-sulfuric acid method was also carried out[77]. Compared with the control group (0.4% DMSO), upon the addition of FcP_{15}@β-CD, the resultant EPS yields at four concentrations of 0.5×, 1.0×, 2.0×, $4.0\times EC_{50}$ were 50.39%, 38.89%, 27.22%, and 20.01%, respectively, which were lower than the corresponding 65.68%, 41.95%, 33.50%, and 23.97% in the FcP_{15} treatment groups (Supplementary Fig. 26). This outcome revealed that FcP_{15}@β-CD had stronger inhibitory effect on the EPS production. Following this, we employed q-PCR to assess the expression of *gum* genes in *Xoo* after treatment with the two experimental agents. Supramolecule treatment resulted in a downregulation of 46.93% for *gum B*, 39.04% for *gum E*, 26.04% for *gum G*, and 30.73% for *gum H* at $2.0\times EC_{50}$, exhibiting superior downregulation compared to the guest molecule across all gene subtypes (Fig. 7B and Supplementary Table 2). It is noteworthy that both guest molecules and the supramolecule scarcely influenced *Xoo* cell growth at $2.0\times EC_{50}$. Consequently, both entities inhibit EPS production by suppressing the expression of *gum* gene clusters without compromising cell growth, with the supramolecule displaying superior downregulation and inhibition effects.

Bacterial motility is pivotal in pathogen attachment, biofilm formation, and pathogenicity, and its inhibition or loss impedes biofilm development and diminishes the pathogen's virulence. Thus, we delved deeper into the impacts of both the supramolecule and individual host/guest molecules on *Xoo* motility. As depicted in Fig. 7C, D, the movement diameter of *Xoo* cells notably decreased following supramolecule treatment compared to treatment with individual host/guest molecules, with the movement diameter measuring only 20.50 mm, whereas the range of movement diameters for the other treatment groups varied between 31.75 and 39.25 mm. Gene expression underlying this phenomenon unveiled that following treatment with FcP_{15}@β-CD, the expression levels of swimming-related genes, notably *flg B*, *mot A*, and *mot B*, decreased by 47.62%, 59.58%, and 52.87%, respectively, lower than those observed in the guest molecule treatment group (Fig. 7E). These findings suggest that the supramolecule inhibits bacterial motility by downregulating swimming-related genes, thereby potentially impeding biofilm formation and pathogenicity.

Upon attachment and invasion of rice leaves, *Xoo* secretes extracellular cellulases and amylases, both of which facilitate the degradation of plant cell walls, thereby enabling bacterial entry into the host plant[78–80]. In investigating the impact of the supramolecule and guest molecules on cellulases and amylases (Fig. 7F–H), the levels of cellulases and amylases decreased by 20.85% and 28.36%, respectively, following supramolecule treatment, which was superior to those observed with the guest molecules alone (12.45% for cellulases and 18.55% for amylases). Furthermore, the formation, maturation, and proliferation of biofilms are typically orchestrated by diffusible signal factor (DSF), whose expression levels are governed by the *rpf* gene family[81–83]. Hence, DSF was extracted from the supernatant of *Xoo* cells subjected to treatment with both guest molecules and the supramolecule. Quantitative analysis demonstrated a reduction in DSF production in *Xoo* treated with FcP_{15}@β-CD compared to treatment with the individual guest molecule (Fig. 7I). Moreover, the supramolecule resulted in downregulation in the expression of *rpf* gene family subtypes, namely *rpf B* (38.59%), *rpf F* (55.14%), and *rpf G* (32.41%), surpassing those triggered by the individual guest molecules (Fig. 7J). The attenuation in *Xoo* pathogenicity induced by both the supramolecule and guest molecules was further corroborated through in vivo experiments on rice leaves. Treatment with FcP_{15} and FcP_{15}@β-CD led to a reduction in the length of rice lesions, measuring 12.29 cm and 8.15 cm (Fig. 7K, L), respectively. Notably, supramolecule FcP_{15}@β-CD consistently demonstrated superiority both in vitro and in vivo compared to FcP_{15} alone.

To reveal the development of bacterial resistance to FcP_{15} and FcP_{15}@β-CD, we cultured 1–12 generations of *Xoo* strains under the inducing factor of FcP_{15} at $1\times EC_{50}$ (4.45 μg/mL) to evaluate their differences in EC_{50} values. As displayed in Supplementary Fig. 27, FcP_{15} and FcP_{15}@β-CD gave EC_{50} ranges of 4.48–4.70 μg/mL and 3.82-3.95 μg/mL, respectively. In contrast, TC provided a gradually increased EC_{50} value after the 2nd

https://doi.org/10.1038/s41467-025-57839-x

generation, showing an EC_{50} value from 68.5 μg/mL (the 2nd generation) to 92.2 μg/mL (the 12th generation). This result reveals that the current supramolecular bactericide can reduce the occurrence of bacterial resistance.

Superior in vivo antimicrobial activity against bacterial plant diseases

Our overarching objective is to unearth bactericides endowed with high efficacy, distinguished by improved physicochemical profiles,

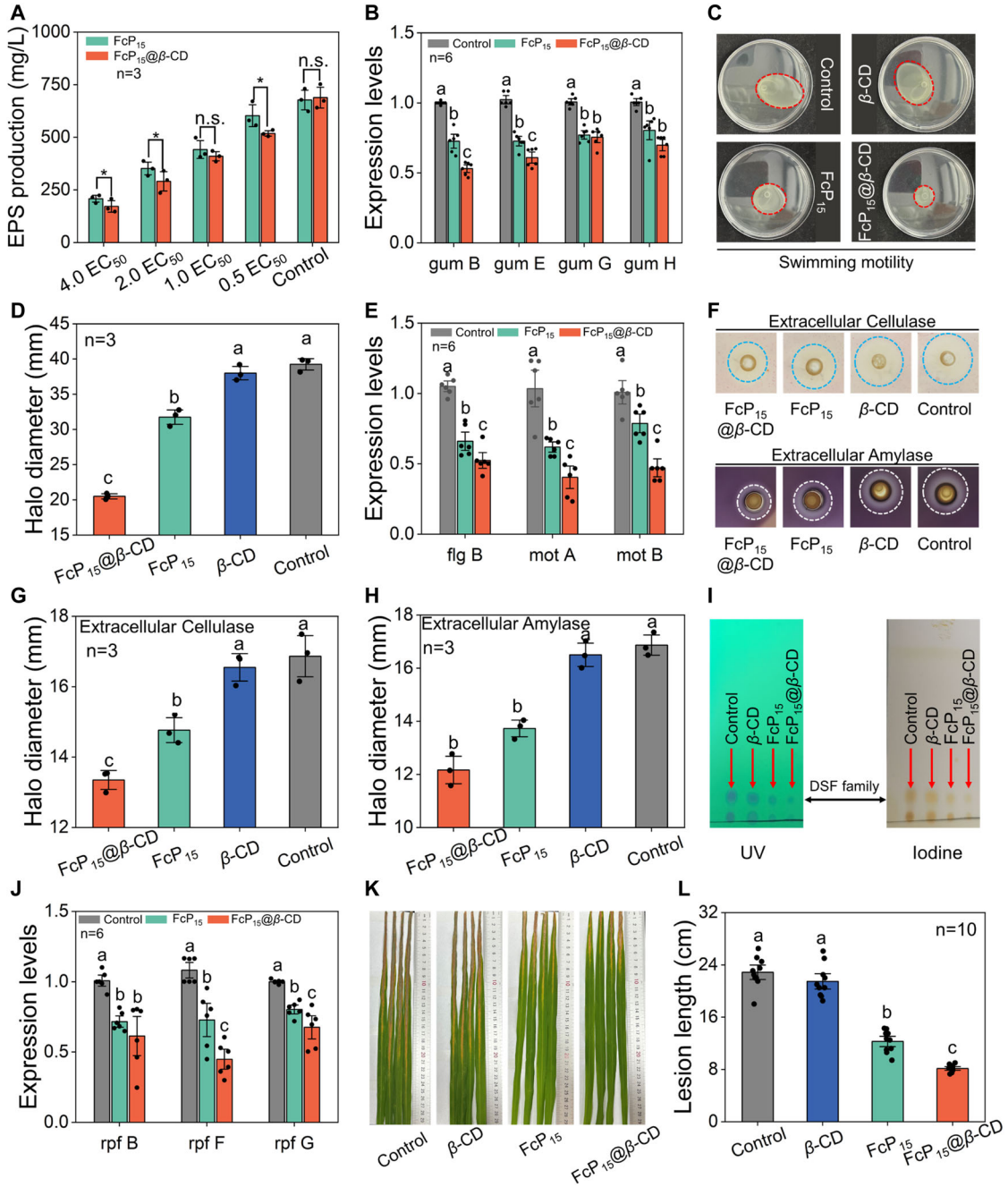

Fig. 7 | The mechanism of action of FcP_{15} and FcP_{15}@β-CD underlying biofilm disintegration. A Induction of EPS yield by FcP_{15} and FcP_{15}@β-CD at different concentrations (from 0.5 to 4.0×EC_{50}). **B** Expression levels of *gum* genes related to EPS synthesis in *Xoo* upon treatment with 2.0×EC_{50} of FcP_{15} and FcP_{15}@β-CD. Swimming motility assays (**C**) and the corresponding diameter of swimming circles (**D**) of *Xoo* following treatment with β-CD, FcP_{15}, and FcP_{15}@β-CD. **E** Gene expression related to the swimming motility of *Xoo* after exposure to 2.0×EC_{50} of FcP_{15} and FcP_{15}@β-CD. **F** Images illustrating extracellular cellulase and extracellular amylase activity, along with circle diameters of extracellular cellulase (**G**) and amylase (**H**) post-intervention with FcP_{15}@β-CD, FcP_{15}, and β-CD. **I** The culture supernatants were used to extract DSF, which was then analyzed by TLC and visualized under UV light at 254 nm and in an iodine chamber. **J** Expression of *rpf* genes involved in DSF production in *Xoo* upon treatment with 2.0×EC_{50} of FcP_{15} and FcP_{15}@β-CD. **K** Representative images of rice leaves infected by *Xoo* through the leaf-clipping inoculation method, treated with β-CD, FcP_{15}, and FcP_{15}@β-CD at 8.90 μg/mL. **L** Quantification of leaf lesion lengths from the aforementioned pathogenicity assay. For panels (**A**, **B**, **D**, **E**, **G**, **H**, **J**, **L**), error bars represent means ± standard error (SE). For (**A**), statistically significant differences between the means were determined using Student's *t*-test, with significance levels indicated as $^{*}p < 0.05$, $^{**}p < 0.01$, and $^{***}p < 0.001$; n.s. denotes no significance. For (**B**, **D**, **E**, **G**, **H**, **J**, **L**), different letters denote statistically significant differences, determined by one-way ANOVA followed by the least significant difference (LSD) post-hoc test analysis ($p < 0.05$). The experiments were conducted with a minimum of three replicates, and the sample size for each data point is specified within the respective figure. Source data are provided as a Source Data file.

thereby necessitating more extensive in vivo experimentation. First, to evaluate the effectiveness of the entities against rice BLB, the leaf-clipping inoculation method was employed (Fig. 8A), which unveiled severe disease symptoms on rice leaves in the control and β-CD groups[84]. Conversely, FcP_{15}@β-CD notably ameliorated disease symptoms at 200 μg/mL, showcasing preventive efficiency (57.83%), surpassing the performance of individual FcP_{15} (46.75%) and the widely used commercial bactericide TC (39.59%) at the same concentration. Considering the effects of supramolecule on *Xoo*-induced BLB and the impressive in vitro potency of the preferred guest molecule and its analogs against *Xanthomonas oryzae* pv. *oryzicola* (*Xoc*) (Supplementary Table 3), another *Xanthomonas* species, we proceeded to evaluate the efficacy of FcP_{15}@β-CD in addressing *Xoc*-induced BLS via a pressure infiltration method (Fig. 8B)[85]. Severe disease symptoms were noted on rice leaves in both the control and β-CD groups, resulting in lesion lengths of 20.3 mm and 19.7 mm, respectively. However, FcP_{15}@β-CD treatment at the same concentration led to a reduction in lesion length to 9.53 mm, achieving a control efficacy of 53.18%, which notably exceeded that of individual FcP_{15} (44.98%) and TC (40.07%). Furthermore, the safety of both the guest molecule and the supramolecule on plants was assessed[86]. Spraying FcP_{15} and FcP_{15}@β-CD at concentrations as high as 500 μg/mL on rice leaves under similar growth conditions resulted in normal growth and healthy leaves across all groups after 7 days (Fig. 8C). This suggests that FcP_{15} and FcP_{15}@β-CD pose no adverse effects on rice, even at doses far exceeding the effective concentration.

To investigate the anti-biofilm and bactericidal duration of FcP_{15}@β-CD and FcP_{15} on rice leaf surfaces, we assessed their in vivo control efficacy against rice leaf blight by inoculating *Xoo* strains on the 1st, 3rd, 5th, 7th, and 10th days after uniformly spraying a 200 μg/mL concentration of the bactericides onto rice leaves. Later, these treatment samples were cultivated for another 14 days to calculate the control efficacy. As presented in Supplementary Fig. 28, FcP_{15}@β-CD showed good durability for controlling rice bacterial blight, affording a control effect of 58.14–49.16%, even after inoculation on the 10th day. This effect was superior to those of FcP_{15} (51.86–40.2%) and TC-20%SC (43.18–31.23%), confirming the better performance of supramolecular materials.

With the impressive prowess demonstrated by FcP_{15} and FcP_{15}@β-CD against BLB and BLS, we embarked on an inquiry into their broad-spectrum antibacterial attributes by evaluating their potential in combating CBC induced by *Xanthomonas axonopodis* pv. *citri* (*Xac*), a member of *Xanthomonas*. Prior to the in vivo assay, we initially assessed the antibacterial potency of the guest molecule against *Xac*. FcP_{15} stood out as one of the most potent compounds against *Xac* (Supplementary Table 3, EC_{50} = 3.28 μg/mL), leading us to anticipate efficacy from the supramolecule derived from it. As depicted in Fig. 9A, B, the control group exhibited numerous prominent yellow circular spots on the citrus leaves. Upon treatment with FcP_{15}@β-CD, this symptom was alleviated, with a preventive efficacy of up to 79.75% at 200 μg/mL, notably surpassing that of the individual FcP_{15} (68.89%) and TC (59.37%). The preventive efficacy may be attributed to well-covered deposition effect of the droplets containing FcP_{15}@β-CD as observed on citrus leaves (Fig. 9C).

Furthermore, both FcP_{15} and the FcP_{15}@β-CD granted vigorous and sustained growth of zebrafishes and earthworms[87], devoid of discernible toxicity, at a concentration of 15 μg/mL (Fig. 9D and Supplementary Fig. 29, criteria: LC_{50} > 10 μg/mL is classified as low toxicity according to Baran Alper[88]), thereby underscoring safety and environmental compatibility of the supramolecular material FcP_{15}@β-CD. Then, the related histopathological analysis of the liver in zebrafish was carried out by hematoxylin staining[89,90]. As illustrated in Supplementary Fig. 30, in the healthy control group, the zebrafish liver tissue is covered by a thin serosa, composed of a single layer of flattened epithelium and a very thin layer of connective tissue. Hepatocytes are arranged in a bilayered, plate-like pattern, with liver plates radiating around the central vein. Hepatic cords appear curved, branched, and interconnected, and hepatocyte nuclei are large and round. In the FcP_{15} and FcP_{15}@β-CD treatment groups, slight hepatocyte degeneration can be observed, with cytoplasmic vacuoles of varying sizes. The liver sinusoids are structurally normal, with no detectable congestion, expansion, or inflammatory cell infiltration observed. The portal areas are clear, with no obvious enlargement, fibrous connective tissue proliferation, or inflammatory cell infiltration. No other pathological changes were noted. Overall, FcP_{15} and FcP_{15}@β-CD treatments did not induce teratogenic effects in zebrafish, nor did they cause pathological toxicity in liver tissue.

The degradation properties of FcP_{15} and FcP_{15}@β-CD and their biological safety to soil microorganisms

The degradation properties of FcP_{15} and FcP_{15}@β-CD on rice leaves were assessed by HPLC measurements. As illustrated in Supplementary Figs. 31, 32, after 10 days of cultivation, the supramolecular material FcP_{15}@β-CD gave relatively lower degradation rates of 4.87%, 11.93%, 14.45%, 19.88%, and 28.08%, on the 1st, 3rd, 5th, 7th, and 10th day, respectively. In contrast, the FcP_{15} itself achieved large degradation rates of 11.64%, 20.33%, 30.53%, 34.88%, and 44.66%, on the 1st, 3rd, 5th, 7th, and 10th day, respectively. This finding reveals that the fabricated supramolecular system is more stable on the rice leaves, providing sustainable protection against bacterial infections.

The biodegradability of FcP_{15}@β-CD and FcP_{15} in chernozem, red ferrallitic, and cambisols soils were assessed by using HPLC measurements at different storage periods (0, 1, 3, 5, 7, and 10 days). In this experiment, FcP_{15}@β-CD and FcP_{15} with a concentration of 50 μg/g were co-incubated with the three soils for 1, 3, 5, 7, and 10 days. After that, all the samples were extracted by methanol and detected by HPLC. The original peak areas at different conditions were provided in Supplementary Figs. 33–35. According to the initial peak area, the related degradation rates were calculated and presented in Supplementary Fig. 36. Clearly, after 10 days of storage in chernozem, red ferrallitic, cambisols soils, the supramolecular complex (FcP_{15}@β-CD) gave relatively high degradation rates of 55.79%, 59.46%, and 60.02%, respectively. Meanwhile, the FcP_{15} itself also showed higher degradation rates of 58.52%, 67.49%, and 62.60%, respectively. This outcome suggests the designed bactericides FcP_{15}@β-CD and FcP_{15} have good biodegradability in different soils, which will be beneficial to ecological safety.

The biological safety of FcP_{15}@β-CD and FcP_{15} to soil microorganisms was illustrated by the amplicon sequencing experiments. FcP_{15}@β-CD and FcP_{15} with a series of concentrations of 0.06, 0.6, and 6 mg/kg were co-incubated with the representative soil for rice cultivation (Supplementary Fig. 37). After that, all the samples were subjected to DNA extraction, PCR amplification and electrophoretic analysis of products, pooling and gel excision purification, and library preparation and sequencing[91]. Based on the achieved results and comprehensive analysis (Supplementary Figs. 38–42), FcP_{15} and FcP_{15}@β-CD have a minimal effect on individual microbial populations and cause small shifts in the overall microbial community structure, preliminarily demonstrating their potential biological safety.

In summary, we have adeptly fabricated a supramolecular material, FcP_{15}@β-CD, leveraging host-guest self-assembly driven by hydrogen bonding and hydrophilic/hydrophobic interactions. Comprehensive characterization via ^{1}H NMR titration, UV–vis spectroscopy, and HRMS unequivocally validate the encapsulation of FcP_{15} within β-CD at 1:1 (molar ratio), exhibiting stable binding, characterized by a binding constant of 1.60×10^4 M^{-1}. Analysis of physicochemical profiles demonstrates the efficacy of FcP_{15}@β-CD in mitigating droplet bouncing and splashing, while simultaneously augmenting wetting behavior, thereby awarding the optimal deposition of FcP_{15}@β-CD onto rice leaf surfaces. Investigations into antibacterial

https://doi.org/10.1038/s41467-025-57839-x

efficacy reveal that FcP_{15}@β-CD adeptly inhibits biofilm formation and effectively disintegrates preformed biofilms in a concentration-dependent fashion, with both inhibitory and disruptive capabilities outperforming those of the individual guest molecule FcP_{15}. The mechanisms underlying biofilm inhibition and disruption unveil its multifaceted actions of FcP_{15}@β-CD. Firstly, by suppressing the expression of the *gum* gene cluster, it inhibits EPS production, thereby impeding biofilm establishment and maintenance. Secondly, through

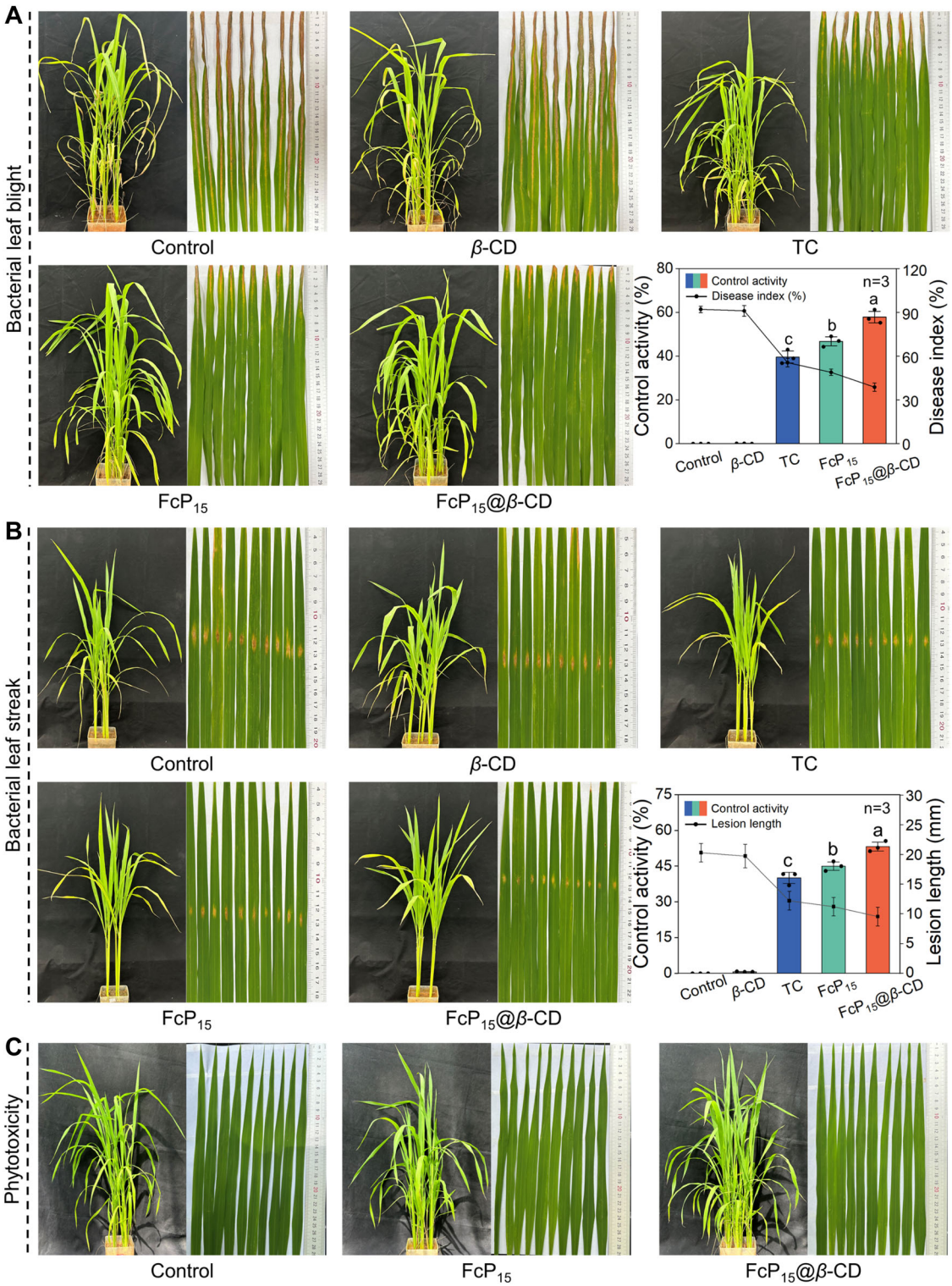

Fig. 8 | In vivo performance of FcP_{15} and FcP_{15}@β-CD against bacterial leaf blight and bacterial leaf streak. A Photographic documentation and assessment of in vivo efficacy of FcP_{15}, FcP_{15}@β-CD, and commercial bactericide TC against rice bacterial leaf blight at 200 μg/mL. **B** Visual representation and assessment of in vivo efficacy of FcP_{15}, FcP_{15}@β-CD, and TC against rice bacterial leaf streak at 200 μg/mL. **C** Evaluation of phytotoxicity of FcP_{15} and FcP_{15}@β-CD on rice plants at 500 μg/mL. In (**A**, **B**), the error bars show the mean ± standard error (SE), with distinct letters indicating significant differences as determined by one-way ANOVA and subsequent least significant difference (LSD) post-hoc testing ($p < 0.05$). The experiments were performed with a minimum of three replicates, and the sample size for each data point is indicated in the respective figure. Source data are provided as a Source Data file.

https://doi.org/10.1038/s41467-025-57839-x

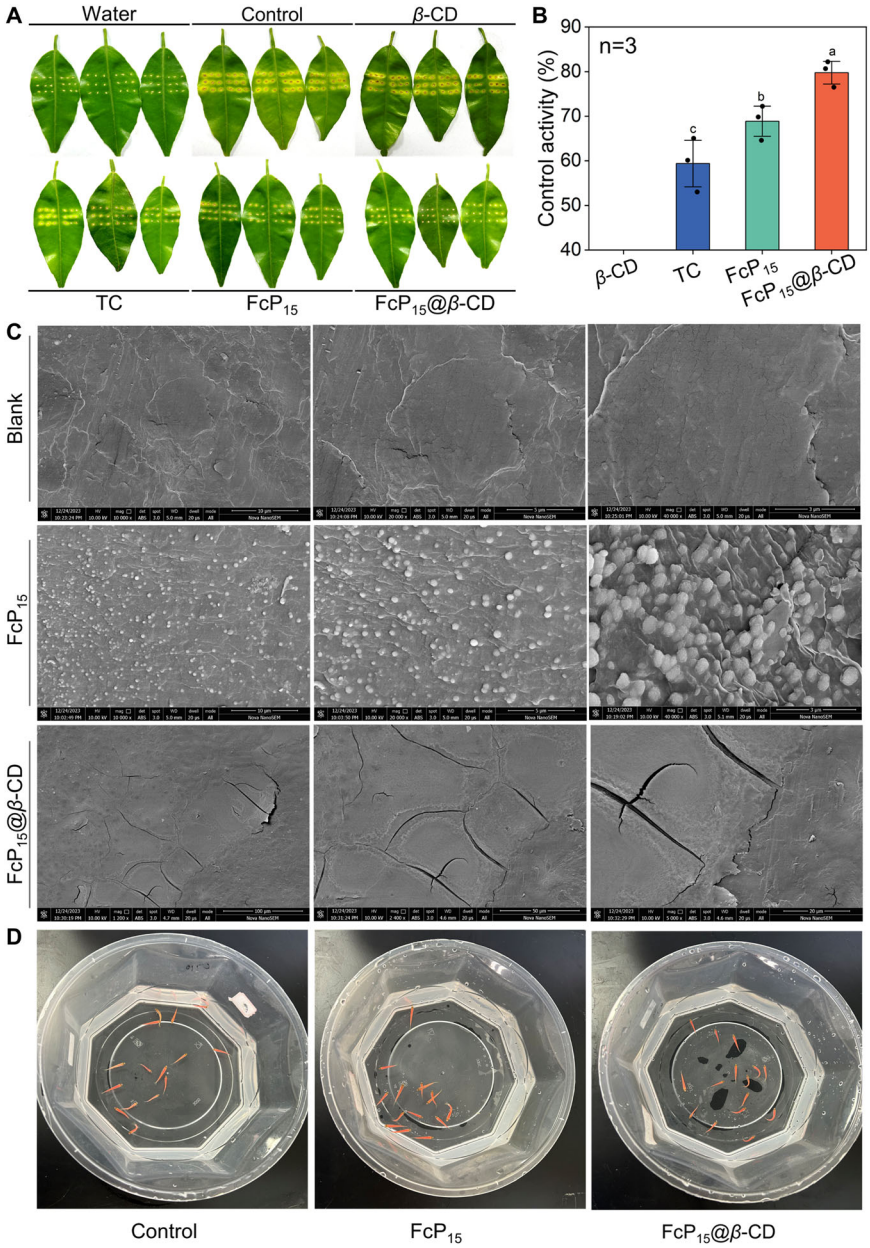

Fig. 9 | The safety of FcP_{15} and FcP_{15}@β-CD towards target and non-target organisms. Visual documentation (**A**) and assessment of in vivo control activity (**B**) of FcP_{15}, FcP_{15}@β-CD, and TC against citrus bacterial canker at 200 μg/mL. **C** SEM images depicting deposition patterns of FcP_{15} and FcP_{15}@β-CD on the citrus leaves. **D** Images of acute toxicity test toward zebrafish captured four days after exposure to control, FcP_{15}, and FcP_{15}@β-CD at 15 μg/mL. For (**B**), error bars indicate the mean ± standard error (SE), with different letters representing statistically significant differences, as determined by one-way ANOVA followed by the least significant difference (LSD) post-hoc test ($n = 3$, $p < 0.05$). The experiments were performed with at least three replicates. Source data are provided as a Source Data file.

the downregulation of swimming-related genes *flg B*, *mot A*, and *mot B*, it curtails bacterial motility, consequently inhibiting biofilm development and bacterial pathogenicity. Thirdly, by attenuating the potency of cellulase and amylase, it weakens the degradation of plant cell walls, thus diminishing invasiveness. Lastly, by downregulating the expression of *rpf* gene family subtypes *rpf B*, *rpf F*, and *rpf G*, it decreases the production of DSF, effectively combating biofilm formation, maturation, and proliferation. Without exception, FcP_{15}@β-CD outperforms the individual guest molecule FcP_{15} across all aforementioned studies. In vivo experiments, FcP_{15}@β-CD showcases the preventive effects against BLB, BLS, and CBC, boasting control efficacies of 57.83%, 53.18%, and 79.75%, respectively, all surpassing those of the commercial bactericide TC. Hence, it is evident that FcP_{15}@β-CD effectively alleviates bacterial-infected plant diseases through its dual action on biofilms, inhibiting their formation and disrupting established ones, thus emerging as a candidate for combating *Xanthomonas* infections. Furthermore, its negligible impact on plants and zebrafish, even at high concentrations, combined with its straightforward and cost-effective preparation procedure, positions it as a supramolecular material with promising applications. More critically, its fabrication eschews additional organic solvents and surfactants, mitigating the undue risks that traditional auxiliaries-assisted pesticides pose to fragile ecosystem, food safety, and human health. In conclusion, FcP_{15}@β-CD emerges as a promising bactericidal material endowed with numerous distinctive advantages in terms of potency, cost-effectiveness, eco-friendliness, and environmental sustainability.

Methods

Synthesis of target compounds FcP_1-FcP_{20}

Preparation of intermediate 1. Ferrocene carboxaldehyde (500 mg, 2.34 mmol), 4-aminophenol (254.92 mg, 2.34 mmol), zinc acetate (12 mg, 0.1168 mmol), and diethyl phosphite (645 mg, 4 mmol) were placed in a 100 mL round-bottom flask and heated under reflux. The reaction was allowed to proceed for 2 h until it was complete. Afterward, 150 mL of a saturated salt solution was added, and the mixture was extracted with 60 mL of dichloromethane. The organic layer was dried over anhydrous sodium sulfate and concentrated under a vacuum. Purification via column chromatography with dichloromethane/methanol (gradient from 100/1 to 50/1, v/v) yielded the desired product (900 mg, 2.03 mmol, 86.53% yield). ^{1}H NMR (400 MHz, $CDCl_3$): δ (ppm) 6.77 (d, J = 12.1 Hz, 2H), 6.70 (d, J = 8.8 Hz, 2H), 4.36 (dd, J = 15.7, 7.4 Hz, 1H), 4.28 (dd, J = 10.0, 1.1 Hz, 2H), 4.17–4.14 (m, 2H), 4.04 (s, 5H), 3.98 (dd, J = 12.8, 5.7 Hz, 2H), 3.90 (dd, J = 13.0, 5.0 Hz, 2H), 1.20 (t, J = 7.1 Hz, 3H), 1.16 (t, J = 7.1 Hz, 3H).

Preparation of intermediate 2. Intermediate 1 (800 mg, 1.8 mmol), epoxy bromopropane (296.66 mg, 2.17 mmol), and potassium carbonate (299.32 mg, 2.17 mmol) were mixed in a 100 mL round-bottom flask and refluxed at 45 °C for 6 h. After that, the mixture was dissolved in 60 mL of ethyl acetate and washed with saturated ammonium chloride solution (80 mL × 3 times). The combined organic layers were concentrated under reduced pressure and the residue was purified using column chromatography with a petroleum ether/ethyl acetate mixture (10/1, v/v), yielding the desired product (600 mg, 1.2 mmol, 66.58%. ^{1}H NMR (500 MHz, $CDCl_3$) δ (ppm) 6.85 (d, J = 9.0 Hz, 2H), 6.77 (d, J = 9.0 Hz, 2H), 4.38 (d, J = 16.1 Hz, 1H), 4.30–4.26 (m, 2H), 4.17–4.14 (m, 2H), 4.04 (s, 5H), 4.01 (d, J = 4.8 Hz, 1H), 3.99 (d, J = 3.0 Hz, 1H), 3.95 (dd, J = 16.4, 6.3 Hz, 2H), 3.90 (dd, J = 11.0, 5.5 Hz, 2H), 3.37–3.29 (m, 1H), 2.92–2.84 (m, 1H), 2.75–2.71 (m, 1H), 1.20 (t, J = 7.1 Hz, 3H), 1.17 (t, J = 7.1 Hz, 3H).

Preparation of target compounds (FcP_1-FcP_{20}). Intermediate 2 (0.4 mmol), assorted substituted primary amines (0.4 mmol), and potassium carbonate (0.6 mmol) were combined in 8 mL of isopropanol and stirred at 50 °C for 24 h in a 15 mL pressure bottle. Following this, the mixture was diluted with ethyl acetate and washed with water. The organic phase was dried over anhydrous sodium sulfate, concentrated, and purified by column chromatography using a dichloromethane/methanol gradient (50/1 to 10/1, v/v) as the eluent, yielding products ranging from 37.3% to 83.7%.

In vitro antibacterial bioassays

The antibacterial efficacy of target compounds and TC against *Xanthomonas oryzae* pv. *oryzae* (*Xoo*), *Xanthomonas oryzae* pv. *oryzicola* (*Xoc*), and *Xanthomonas axonopodis* pv. *citri (Xac)* was evaluated using a turbidimetric method. Briefly, 40 µL of bacterial suspension (OD_{595} = 0.6–0.8) was introduced into 5.0 mL of nutrient broth composed of 1.0 g yeast powder, 3.0 g beef extract, 5.0 g peptone, and 10.0 g glucose per liter of deionized water (pH 7.2), supplemented with various concentrations of the compounds. In addition, 0.4% DMSO and 0.1% tween-80 were dissolved in nutrient broth to improve the water-solubility of synthesized compounds. Samples were then incubated in a shaker at 180 rpm and 28 °C for 36–48 h until the turbidity of the negative control (equivalent amount of DMSO) reached an OD_{595} value of 0.6. For each sample, 200 µL was transferred to a 96-well plate to measure turbidity, where the corrected value was calculated as $OD_{\text{bacterial wilt}} - OD_{\text{no bacterial wilt}}$. The final growth inhibition rate (I) was determined using the formula:

$$I(\%) = \frac{C - T}{C} \times 100 \quad (1)$$

Where C corresponds to the adjusted turbidity values for the control, and T corresponds to the adjusted turbidity values for the test samples. The EC_{50} values were calculated using Microsoft Excel 2019, based on the inhibition rates observed at various concentrations. Every test was conducted in triplicate.

Preparation and characterization of the complex FcP_{15}@β-CD

NMR spectra. The assembly behavior and driving forces of FcP_{15} and β-cyclodextrin (β-CD) in D_2O were investigated using ^{1}H NMR spectroscopy. For this analysis, solutions containing 5.0 mM of FcP_{15}, β-CD, and their inclusion complexes were prepared in different molar ratios (1:0, 1:1, and 1:2, respectively) and characterized by ^{1}H NMR to assess the interactions and complexation efficiency.

Ultraviolet spectroscopic analysis. β-cyclodextrin (β-CD) was incrementally added to a fixed concentration of FcP_{15} at 0.1 mM. The absorption intensity of the characteristic peak was monitored continuously until the addition of β-CD reached 2.0 equivalents. Prepare FcP_{15} and FcP_{15}@β-CD with different concentrations, using the instrument to test the UV absorption spectrum. First, make water with different volume ratios of methanol solution 3 mL, then join the concentration of FcP_{15} and FcP_{15}@β-CD 0.25 mM, respectively, after the shake test its ultraviolet absorption.

High-performance liquid chromatography (HPLC). The contents (peak area) of FcP_{15} and FcP_{15}@β-CD were ascertained by HPLC (Conditions: XDB-C_{18} 4.6 × 150 mm × 5 µm, acetonitrile/water (0.5% formic acid) = 45/55, 1.0 mL/min, injection volume 10.0 µL, λ = 245 nm, Rt = 2.974–3.428 min).

Contact angle assessment. Following the meticulous preparation of an aqueous solution of β-CD, FcP_{15}, and FcP_{15}@β-CD (200 µg/mL), alongside water serving as the control, a contact angle test was conducted. Laboratory-cultivated rice leaves were delicately positioned on a slide, upon which 10 µL droplets of each solution were precisely dispensed using a micro syringe. The contact angles were then measured using a JC 2000D1 contact angle instrument, with each solution tested thrice on different sections of the leaf.

Zeta potential determination. The FcP_{15} and FcP_{15}@β-CD were dissolved with 200 µg/mL. After different storage times of solutions, the Zeta potential was measured using a dynamic light scattering instrument.

Wettability and adhesion ability. Wettability and adhesion on fresh rice foliage were assessed using 1.0 cm diameter leaf disks, excised using a hole puncher and immersed in solutions of 200 µg/mL FcP_{15}, FcP_{15}@β-CD, β-CD, and 0.4% DMSO for 15 s. Subsequently, the disks were gripped with tweezers, allowing any excess liquid to drip off until no droplets remained. The weight of each disk was then precisely measured with an analytical balance. The liquid holding capacity (LHC) of the samples on the leaf surface was calculated using the formula $LHC = (M_1 - M_0)/S$, where M_0 and M_1 represent the weights of the leaf discs before and after immersion, respectively, and S is the surface area of the leaves. All samples were tested in triplicate in this assay.

Liquid surface tension test. The samples FcP_{15}, β-CD, and FcP_{15}@β-CD were prepared as aqueous solutions with 200 µg/mL, and their surface tension was ascertained using the drop-weight method. The experiment was conducted at room temperature. Samples were drawn into a contamination-free syringe and placed within a JC 2000D1 contact angle instrument. The measurement commenced with a minimal extrusion of liquid to mitigate the effects of external phase diffusion, followed by a gradual release. Once the suspended liquid droplets reached their maximum volume, the image was captured. Surface

tension was then calculated using the built-in data analysis function of the instrument.

Droplet splashing and bouncing experiment. The behaviors of water, β-CD, FcP_{15}, and FcP_{15}@β-CD solutions on rice leaf surfaces were analyzed by using a high-frame-rate camera with each solution being prepared at 200 μg/mL. The impacts of the droplets were visually recorded and compared to assess their splashing (from a height of 35 cm release) and bouncing (from a height of 10 cm release) characteristics. The process was documented and data analyzed using i-SPEED Suite software, providing detailed insights into the dynamic interactions.

Investigation of the antibacterial mechanism

Growth of *Xoo* biofilm assessment. The cultured *Xoo* bacterial suspension was diluted to an OD_{595} of 0.1 using Nutrient Broth (NB) medium. Then, 200 μL of the suspension was added to sterilized 96-well plates and incubated in a shaking incubator (28 °C, 180 rpm). After incubation for corresponding 24, 36, 48, and 60 h, their OD_{595} values for *Xoo* solutions were measured, and floating bacteria were removed. Then, 200 μL of 0.1% crystal violet dye was added to each well for staining for 30 min. After removing the dye, the wells were washed with water three times and left to air dry. Finally, the biofilm was dissolved in 95% ethanol, and the OD_{570} value was measured for biofilm quantification.

Biofilm inhibition assay. The *Xoo* bacterial solution (OD_{595} = 0.6–0.8) was resuspended and adjusted to OD_{595} of 0.1 using sterilized NB medium. This solution (200 μL) was then transferred into a sterile 96-well plate. Various concentrations of 0.4% DMSO, compound FcP_{15}, and the inclusion complex FcP_{15}@β-CD were added at 8.0 × EC_{50}, 4.0 × EC_{50}, 2.0 × EC_{50}, 1.0×EC_{50}, and 0.5×EC_{50}. After incubating at 28 °C for 48 h, discard the culture medium and wash the wells with water to remove any unattached bacteria. Then, add 200 μL of 0.1% crystal violet stain to each well and stain for 30 min. Wash the wells with sterile water and allow them to air dry. Finally, dissolve the stained biofilm in 200 μL of 95% ethanol and measure the OD_{570} to quantify the biofilm production.

Growth curve of *Xoo*. The overnight culture of *Xoo* bacteria was resuspended and the optical density at 595 nm was adjusted to 0.1 using sterilized NB medium. A quantity of 40 mL of this adjusted bacterial solution was transferred into a 100 mL conical flask, to which either 0.4% DMSO or FcP_{15} was added. The concentration of FcP_{15} in the bacterial suspension was set at incremental levels of 0.5–8 × EC_{50}, each in 1.0 mL aliquots in test tubes. These samples were incubated at 180 rpm in a shaker at 28 °C. The OD_{595} was measured at 3-h intervals over a period of 36 h, with each measurement conducted in triplicate.

Destruction of pre-established biofilms. Bacterial species were incubated in a 96-well flat-bottom plate at 28 °C for 48 h to allow biofilm formation. Post-incubation, the biofilms were washed twice with phosphate-buffered saline (PBS). A pre-mixed solution of NB and FcP_{15}, as well as the inclusion complex FcP_{15}@β-CD at varying concentrations, was added to each well. The biofilms were treated for 16 h, after which the NA solution was removed, and the biofilms were washed thrice with 200 μL PBS to eliminate planktonic cells. Following the protocol used in previous biofilm inhibition assays, each well was stained with 200 μL of 0.1% crystal violet for 30 min, then the dye was removed, and the wells were washed thrice with sterile water and air-dried. Biofilm quantification was achieved by dissolving the retained crystal violet with 95% ethanol (200 μL) and recording the absorbance (OD_{570}).

Measurement of confocal laser scanning microscopy (CLSM). Sterilize glass slides (10 × 10 mm) and place them in a six-well plate. Add 8.0 mL of *Xoo* bacterial suspension (OD_{595} = 0.1) and incubate at 28 °C for 48 h. Then, add different concentrations of FcP_{15} and FcP_{15}@β-CD to the wells and continue incubating overnight at 28 °C. Afterward, remove the planktonic bacteria from the supernatant and stain with 0.1% AO and then with 0.01% PI. All samples were observed using a confocal laser scanning microscope (CLSM) with 488 or 543 nm lasers.

Biofilm-associated *Xoo* colony formation assay. Sterilized glass slides (10 × 10 mm) were placed in six-well plates. Then, *Xoo* suspension (OD_{595} = 0.1, 8.0 mL) was added to each well, followed by the addition of different concentrations of FcP_{15} and FcP_{15}@β-CD. After incubation for 48 h, discard the culture medium and supplement PBS buffer (1.0 mL). Then, the system was subjected to ultrasonic treatment to obtain a uniform *Xoo* bacterial suspension, which is then diluted 10^5 times and plated on nutrient agar plates. After incubation for 3 d at 28 °C, take pictures and count the colonies formed in each treatment group.

SEM analysis. Glass slides (10 × 10 mm) were autoclaved and placed in a six-well plate. 8.0 mL of *Xoo* bacterial suspension (OD_{595} = 0.1) was added, and the culture was incubated for 48 h. The experiment was then repeated with various concentrations of FcP_{15} and FcP_{15}@β-CD added to pre-formed biofilms, followed by overnight incubation at 28 °C. The slides from each treatment group were rinsed with phosphate-buffered saline, fixed in glutaraldehyde, dehydrated through an ethanol gradient, freeze-dried, and then examined using scanning electron microscopy (SEM).

Quantification assay of exopolysaccharides (EPS). The *Xoo* suspension with OD_{595} = 0.1 was added to NB medium containing different concentrations of each treatment group (0.5 × EC_{50}, 1.0 × EC_{50}, 2.0 × EC_{50}, and 4.0 × EC_{50}), and cultured on a shaking incubator at 28 °C and 180 rpm for 3 d. Afterward, the supernatant was collected by centrifugation, mixed thoroughly with 95% ethanol, and allowed to stand at 4 °C overnight. Finally, the EPS precipitate was obtained by centrifugation and its dry weight was measured. Each condition was performed in triplicate.

Swimming motility assay. Sterile plates were prepared using 0.5% agar, 0.3% beef extract, 0.5% peptone, 1% glucose, and 0.1% yeast extract. *Xoo* suspension with OD_{595} = 1.0 was placed at the center of the plates, followed by treatment with FcP_{15} and FcP_{15}@β-CD at 2.0×EC_{50}. The plates were incubated at 28 °C for 72 h, and the colony diameters of each treatment group were measured at the end.

Cellulase measurements. *Xoo* solution (OD_{595} = 0.5, 1.0 mL) was added into a sterile 2.0 mL centrifuge tube. Subsequently, equivalent doses of FcP_{15} and FcP_{15} encapsulated in β-CD (2.0 × EC_{50}) were added, and the mixture was allowed to incubate for 60 min. Sterile NA plates were prepared with 0.5% carboxymethyl cellulose and then treated with 2.0 μL *Xoo* solution prepared above. The plates were subsequently incubated at 28 °C for 72 h. Following incubation, the plates were stained with a 0.1% Congo red solution for 30 min, followed by a single rinse with sterile water, and subsequent treatment with a 1.0 mol/L sodium chloride solution. The hydrolysis areas of every treatment were then assessed and documented using imaging techniques to ascertain their inhibitory activity.

Amylase activity determination. The *Xoo* suspension was diluted with NB medium to OD_{595} = 0.5, 1.0 mL was transferred to a centrifuge tube, and equal volumes of FcP_{15} and FcP_{15}@β-CD (2.0 × EC_{50}) were added and incubated for 60 min. Then, NA plates (containing 0.1% starch) were made, and 2.0 μL of the treated *Xoo* suspension was inoculated onto the plates. After incubation, *Xoo* cells were cleaned with ethanol

(70%) and stained with 1% iodine/potassium iodide solution. Finally, the hydrolysis cycles and inhibitory activity were assessed through measurements and imaging.

Diffusible signal factor (DSF) extraction and analysis. The *Xoo* bacterial suspension was inoculated into NB medium, with 2.0×EC_{50} concentrations of FcP15 and FcP_{15}@*β*-CD added. The culture was incubated at a shaking incubator (28 °C, 180 rpm) for 16 h. Afterward, the culture was centrifuged to collect the supernatant, and the pH was adjusted to 4.0. Equal volumes of ethyl acetate were used for extraction, followed by concentration using a rotary evaporator and dissolution in 0.5 mL methanol. Then, 2 µL of the sample was applied, and separation was performed using a solvent mixture of hexane, diethyl ether, and acetic acid (8:2:0.1) on a thin-layer chromatography plate. Finally, the plate was observed under 254 nm UV light or visualized with iodine under daylight.

Reverse transcription-quantitative PCR test (RT-qPCR). *Xoo* cell suspensions were treated with 0.4% DMSO or 2.0×EC_{50} concentrations of FcP_{15} and FcP_{15}@*β*-CD, and incubated at a shaking incubator (28 °C, 180 rpm) for 16 h. After incubation, *Xoo* cells were collected by centrifugation and RNA was extracted using the TransZol Up kit. The RNA was reverse transcribed into cDNA using TaKaRa reagents, with gyrB as an internal control for normalization. RT-qPCR was carried out on the iCycler iQ system (Bio-Rad) with SYBR Premix Ex TaqII reagents. Relative expressions were calculated using the $2^{-\Delta\Delta Ct}$ method. Each group has three repetitions.

Pathogenicity test. Rice plants at the tillering stage were selected. *Xoo* cells were adjusted to an OD_{595} of 0.6 and incubated for 12 h in solutions containing 2.0×EC_{50} concentrations of *β*-CD, FcP_{15}, and FcP_{15}@*β*-CD, with 0.4% DMSO as the negative control. The leaf-cutting inoculation method was then used to introduce the *Xoo* cell suspension onto rice leaves. Fourteen days post-inoculation, lesion lengths on the rice leaves were measured, and the results were statistically analyzed using one-way analysis of variance (ANOVA) to determine the effects of each treatment.

Electrical conductivity analysis. *Xoo* cells with OD_{595} = 0.6–0.8 were collected and washed with 5% glucose solution until the conductivity matched that of the glucose solution, forming the bacterial isotonic solution. The isotonic solution was then heated to boiling, while FcP_{15} and FcP_{15}@*β*-CD were added to the 5% glucose solution. Subsequently, various doses of FcP_{15} and FcP_{15}@*β*-CD were moved to the bacterial isotonic solution and incubated at 28 °C, 180 rpm for 8 h, with conductivity measured every hour. The relative electrical conductivity for each group was calculated using the following formula:

$$\frac{L_2 - L_1}{L_0} \quad (2)$$

where L_0 is the conductivity of the isotonic solution after boiling, L_1 is the conductivity after adding FcP_{15} and FcP_{15}@*β*-CD to the 5% glucose solution, and L_2 is the conductivity measured every hour after adding FcP_{15} and FcP_{15}@*β*-CD to the bacterial isotonic solution.

ROS detection and analysis. The *Xoo* suspension (OD_{595} = 0.1) was treated with different concentrations of FcP_{15} and FcP_{15}@*β*-CD (0 ~ 8.0×EC_{50}) at 28 °C for 12 h. Then, *Xoo* cells were collected by centrifugation (3250 g, 3.5 min, 4 °C) and washed twice with water. Next, 100 µL of the bacterial suspension was incubated with 1.0 µL of S0033 dye at 28 °C for 20 min. Fluorescence measurements were performed using a Fluoromax-4cp instrument (excitation wavelength: 488 nm). ROS content was measured using the ROS assay kit (S0033, Beyotime, Shanghai).

Enzyme activities analysis. The *Xoo* bacterial solution (OD_{595} = 0.6–0.8) was first diluted to an OD_{595} of 0.1 using sterilized nutrient broth (NB). The *Xoo* was then treated with different concentrations of FcP_{15} and FcP_{15}@*β*-CD (from 0.0 EC_{50} to 8.0 EC_{50}) and incubated at 28 °C for 12 h at 180 rpm. After centrifugation (6500 *g*, 3.5 min, 4 °C), the cells were harvested and washed with precooled phosphate-buffered saline (PBS, pH = 7.2). The extract provided by the kit was added to the bacteria, followed by sonication (30% power, 3 s ultrasound, 10 s interval, repeated 20 times at 0 °C). Finally, the samples were centrifuged at 8000 *g* for 10 min, and the supernatants were collected. The activities of CAT and SOD in the supernatant were measured according to the kit instructions. The CAT and SOD assay kits were obtained from Solarbio Life Sciences.

EPS quantification using the phenol-sulfuric acid method. *Xoo* cell suspensions (OD_{595} = 0.1) were cultured in NB medium containing various concentrations of FcP_{15} and FcP_{15}@*β*-CD (from 0.5 × EC_{50} to 4.0 × EC_{50}) at 28 °C with shaking at 180 rpm for 3 d. After incubation, the supernatant was collected by centrifugation and mixed with three volumes of 95% ethanol, then left at 4 °C overnight to allow EPS precipitation. The precipitate was re-dissolved in ddH_2O, resulting in a crude sugar solution.

Preparation of glucose standard curves: 0.5 mL glucose solution of 0, 10, 20, 30, 40, 60, and 80 µg/mL was added to seven test tubes (standard), and 2 mL anthrone reagent was added to the test tube, which was immersed in ice water to cool, shaken well, and then immersed in a boiling water bath for 10 min. After cooling to room temperature, under the wavelength of 620 nm, the tube containing 0 µg/mL glucose was used as a blank, and the remaining absorbance values were determined. The glucose content (µg) was used as the abscissa, and the absorbance value was used as the ordinate to make the standard curve. Determination of exopolysaccharide samples: Add 0.5 mL crude sugar solution to the test tube, then immediately add 2.0 mL anthrone reagent, and then the operation steps according to the same method of making standard curve, determine the absorbance, according to the standard curve to calculate the content of exopolysaccharide at different concentrations of each sample. Three parallel experiments at each concentration.

Bacterial resistance studies to supramolecular bactericides. To explore the development of bacterial resistance to current supramolecular bactericides, we used 1–12 generations of *Xoo* strains cultured with compound FcP_{15} at a concentration of 1×EC_{50} (4.45 µg/mL) to test the change of their EC_{50} values, while the commercial bactericide—TC was used as a positive control. The first generation of *Xoo* was added to a new medium (30 mL) with OD_{595} adjusted to 0.1, to which FcP_{15} (0.04% DMSO) at a concentration of 4.45 µg/mL was added, and put into a shaker to continue incubation of the second generation ($OD_{595\ nm}$ = 0.6–0.8), and the operation of the next generation was continued in a similar way, and the bacterial incubation process was repeated for a total of 12 generations.

Phytotoxicity assay to target plants. The FcP_{15} and FcP_{15}@*β*-CD solutions (500 *µ*g/mL) were evenly sprayed on the rice leaves, ensuring complete coverage of each leaf. At the same time, a 0.4% DMSO solution was used as a negative control to eliminate any potential effects of the solvent on the plants. The treated plants were then transferred to a greenhouse for cultivation under suitable temperature and humidity conditions. After 7 d of growth, corresponding lesion symptoms were assessed and recorded periodically.

Toxicity assay on zebrafish. In the toxicity test, zebrafish were placed in static water conditions and not fed. Concentrations of 15 µg/mL of both FcP_{15} and FcP_{15}@*β*-CD were prepared, with 0.4% DMSO used as the negative control. Each treatment group contained 15 fishes.

Mortality was recorded at 24-h intervals, and any deceased fish were promptly removed.

Pathological examination of zebrafish liver tissue. The fixed tissue was dehydrated using an automatic dewatering machine with ethanol solutions of different concentrations (75–100%). Afterward, the tissue was treated with clearing agents I and II for 25 min each, and paraffin I and II for 30 min each, followed by paraffin III treatment for 1 h. The tissue was then embedded and sectioned. After deparaffinization and hydration, the tissue was stained with hematoxylin for 5 min and then washed with deionized water. The cells were differentiated in hydrochloric acid alcohol solution for 3 s, followed by washing with tap water. A weak alkaline solution was used to restore the blue color, and the tissue was rinsed again with tap water. Finally, the tissue was stained with eosin for 3 min, dehydrated in gradient alcohol, cleared with a clearing agent, and mounted with neutral gum.

The amplicon sequencing experiments for the assessment of biological safety of FcP_{15}@β-CD and FcP_{15} to soil microorganisms. The representative soil for rice cultivation (from Huaxi District, Guiyang, Guizhou province) was used and incubated in a thermostatic incubator for 14 days. Then, FcP_{15}@β-CD and FcP_{15} with a series of concentrations of 0.06, 0.6, and 6 mg/kg were co-incubated with the rice soil for another 10 days, while the same amount of 0.4% DMSO aqueous solution was used as the control group. The soil samples were incubated at 20 ± 2 °C in the dark, with a humidity of 80%. During the experiment, the soil moisture content was maintained between 40% and 60% of the field capacity, with a variation range of ±5%. Distilled water or deionized water was added if necessary to adjust the moisture level. After that, all the samples were carried out for DNA extraction, PCR amplification and electrophoretic analysis of products, pooling and gel excision purification, and library preparation and sequencing. There are three repetitions in each group.

DNA extraction. Genomic DNA was isolated from various sample types using suitable extraction kits (for detailed information, refer to the respective technical support). The DNA purity and concentration were then determined using a Nanodrop One instrument (Thermo Fisher Scientific, MA, USA).

PCR amplification and electrophoretic analysis of products. PCR amplification was carried out using genomic DNA as the template, targeting the selected sequencing regions, with specific primers containing barcodes and Premix Taq.

Pooling and gel excision purification. After determining the concentrations of PCR products with GeneTools Analysis Software (Version 4.03.05.0, SynGene), the necessary volume for each sample was calculated based on the equal mass principle and then mixed. Subsequently, the PCR reaction mixture was purified using the E.Z.N.A.® Gel Extraction Kit (Omega, USA), ensuring the removal of any contaminants. The target DNA fragments were then eluted in TE buffer to maintain their purity and concentration for further experimental analysis.

Library preparation and sequencing. Library construction was carried out following the standard protocol of the ALFA-SEQ DNA Library Prep Kit. The size distribution of the library fragments was assessed using the Qsep400 High-Throughput Nucleic Acid & Protein Analysis System (Hangzhou Houze Biotechnology Co., Ltd., China), ensuring the integrity and uniformity of the library. The library concentration was quantified using a Qubit4.0 fluorometer (Thermo Fisher Scientific, Waltham, USA). The prepared amplicon libraries were then subjected to PE250 sequencing on either the Illumina or MGI platforms (Guangdong Magigene Biotechnology Co., Ltd., Guangzhou, China), ensuring the generation of high-quality sequencing data for further analysis. All sequencing processes were carried out in strict accordance with standard protocols to guarantee the accuracy and reliability of the data, providing high-quality foundational data for subsequent analysis.

In vivo assessment of treatments for rice bacterial blight, bacterial leaf streak, and citrus bacterial canker

In vivo anti-*Xoo* efficacy. Rice plants were treated with FcP_{15}, FcP_{15}@β-CD, and TC−20% SC (200 μg/mL). After 24 h, a 2 cm diagonal incision was made at the tip of the leaf using sterilized scissors, and the wound was immersed in an *Xoo* cell suspension (OD_{595} = 0.8) for infection. All the samples were cultured at 28 °C (90% humidity) for 14 d. The disease index and control efficacy were calculated based on the diseased area using the designated formula.

According to the severity level of symptoms and the prescribed formula, the corresponding disease index (*C* and *T* stand for negative and treatment groups, respectively) was obtained for each group:

$$\text{Disease index}(C \text{ or } T) = \sum \frac{(\text{Number of leaves at eachgrade} \times \text{Correspondinggrade})}{(\text{Total number of leavesthe superlative grade})} \quad (3)$$

The following equation was used to assess the anti-*Xoo* efficacy:

$$\text{Control efficacy } I = \frac{C - T}{C} \times 100\% \quad (4)$$

In vivo anti-bacterial leaf streak (ant-BLS) activity. To evaluate the protective and curative efficacy of FcP_{15} and FcP_{15}@β-CD against rice BLS, the pressure infiltration method was employed in vivo pot culture experiments. Initially, rice plants were sprayed with a 200 μg/mL solution of the agents. After 24 h, *Xoc* was inoculated using a needleless syringe. The treated rice was then incubated in a greenhouse chamber for 14 days. Throughout these in vivo experiments, a 0.1% DMSO aqueous solution served as the negative control, while TC was used as the positive control. The length of lesions on the rice leaves was measured, and the control efficacy *I* was calculated according to the formula (*C* and *T* stand for negative and treatment groups, respectively):

$$\text{Control efficacy } I = \frac{C - T}{C} \times 100\% \quad (5)$$

In vivo efficacy evaluation against citrus bacterial canker. In this section, TC 20%SC, serving as the positive control, and an equivalent volume of DMSO (0.4%), used as the blank control, were applied in the antibacterial efficacy test on citrus leaves. Initially, citrus leaves were washed with sterile water and air-dried. Each leaf then had 18 uniformly spaced wounds created in the central area using a sterilized syringe. Solutions of FcP_{15}, FcP_{15}@β-CD, and TC, each at a concentration of 200 μg/mL, along with 0.4% DMSO, were uniformly applied to the wounds until solution dripped from the leaves. After 24 h, filter papers soaked in *Xac* bacterial suspensions at logarithmic growth phase were attached to each wound. The experiments were conducted inside a climate chamber maintained at 95% relative humidity with a light cycle of 28 °C for 16 h and a dark cycle of 25 °C for 8 h. Observations were recorded 14 days post-inoculation and each treatment was replicated in three separate experiments. For analysis, the diseased sections of each leaf were uniformly cut into 100 mg samples. Chlorophyll was then extracted using a mixture of 95% acetone and 95% ethanol in a 1:1 ratio. The absorbance was measured at wavelengths of 663 nm and 645 nm, and the data were subsequently analyzed using the specified formulas (*C* and *T* stand for negative and treatment groups,

respectively):

$$\text{Chlorophyll a} = (12.7 \times OD_{663} - 2.69 \times OD_{645}) \times 0.1 \quad (6)$$

$$\text{Chlorophyll b} = (22.9 \times OD_{645} - 4.68 \times OD_{663}) \times 0.1 \quad (7)$$

$$\text{Total chlorophyll} = (8.02 \times OD_{663} + 20.21 \times OD_{645}) \times 0.1 \quad (8)$$

$$\text{Infected area} = \text{Total chlorophyll of water} - \text{Total chlorophyll of component} \quad (9)$$

$$\text{Control efficacy } I = (C - T)/C \times 100\% \quad (10)$$

Statistics and reproducibility

Statistical analyses were performed using IBM SPSS Statistics 26 and Origin 2021 for Windows. Unless otherwise noted, the data presented in the figures are expressed as the mean ± standard error (SE). All experiments were conducted with no fewer than three replicates with similar results, and the sample size corresponding to each data point is specified within the respective figure. To compare two experimental groups, Student's *t*-test was used, while one-way ANOVA was applied to identify differences among multiple groups. In such cases, the least significant difference post-hoc test was used for pairwise comparisons, as indicated in the figure legends. It should be noted that all statistical tests conducted in this study were two-sided.

Supporting information

The supplementary information includes details on chemicals and instruments, experimental results, as well as the NMR and HRMS spectra for the target compounds.

Reporting summary

Further information on research design is available in the Nature Portfolio Reporting Summary linked to this article.

Data availability

All data supporting the findings of this study are presented within the main text and supplementary files. The compounds, including their numbering, state, color, and spectroscopic analysis (^{1}H, ^{13}C, ^{31}P NMR), are meticulously documented in the Supplementary Information. For any further information, inquiries should be addressed to the corresponding authors, who will readily provide the required details. Source data are provided in this paper. Source data is available for Figs. 1–9 and Supplementary Figs. 1–42 in the associated source data file. Source data are provided in this paper.

References

1. Toushik, S. H. et al. Pernicious attitude of microbial biofilms in agri-farm industries: acquisitions and challenges of existing antibiofilm approaches. *Microorganisms* **10**, 2348 (2022).
2. Fan, G. et al. Antimicrobial mechanisms of ZnO nanoparticles to phytopathogen Pseudomonas syringae: damage of cell envelope, suppression of metabolism, biofilm and motility, and stimulation of stomatal immunity on host plant. *Pestic Biochem Phys* **194**, 105455 (2023).
3. Shamim, A. et al. Natural medicine a promising candidate in combating microbial biofilm. *Antibiotics-Basel* **12**, 299 (2023).
4. Han, S. W. et al. An efficient method for visualization and growth of fluorescent *Xanthomonas oryzae* pv. *oryzae* in planta. *BMC Microbiol* **8**, 164 (2008).
5. Ham, Y. & Kim, T. J. Anthranilamide from *Streptomyces* spp. inhibited *Xanthomonas oryzae* biofilm formation without affecting cell growth. *Appl. Biol. Chem.* **61**, 673 (2018).
6. Vishakha, K. et al. Allelochemical catechol comprehensively impedes bacterial blight of rice caused by *Xanthomonas oryzae* pv. *oryzae*. *Microb. Pathogenesis* **149**, 104559 (2020).
7. Carezzano, M. E. et al. Biofilm-forming ability of phytopathogenic bacteria: a review of its involvement in plant stress. *Plants* **12**, 2207 (2023).
8. Cheng, J. et al. Biofilm heterogeneity-adaptive photoredox catalysis enables red light-triggered nitric oxide release for combating drug-resistant infections. *Nat. Commun.* **14**, 7510 (2023).
9. Dieltjens, L. et al. Inhibiting bacterial cooperation is an evolutionarily robust anti-biofilm strategy. *Nat. Commun.* **11**, 107 (2020).
10. Kalia, V. C., Patel, S. K. & Lee, J. K. Bacterial biofilm inhibitors: an overview. *Ecotox. Environ. Safe.* **264**, 115389 (2023).
11. Basak, A., Abouelhassan, Y. & Huigens, R. W. III Halogenated quinolines discovered through reductive amination with potent eradication activities against MRSA, MRSE and VRE biofilms. *Org. Biomol. Chem.* **13**, 10290–10294 (2015).
12. Garrison, A. T. et al. Bromophenazine derivatives with potent inhibition, dispersion and eradication activities against Staphylococcus aureus biofilms. *RSC Adv.* **5**, 1120–1124 (2015).
13. Du, X. et al. Synthesis of cationic biphen [4, 5] arenes as biofilm disruptors. *Angew. Chem. Int. Edit.* **135**, e202301857 (2023).
14. Guo, S. et al. Synthesis and bioactivity of guanidinium-functionalized pillar [5] arene as a biofilm disruptor. *Angew. Chem. Int. Edit.* **60**, 618–623 (2021).
15. Chen, W. et al. An adjuvant that increases the adhesion of pesticides on plant surfaces and improves the efficiency of pest control: polyethylene glycol sol-gel polymer. *React. Funct. Polym.* **192**, 105722 (2023).
16. Liu, Z. et al. Janus nanoparticles targeting extracellular polymeric substance achieve flexible elimination of drug-resistant biofilms. *Nat. Commun.* **14**, 5132 (2023).
17. He, L. et al. Regulating the entire journey of pesticide application on surfaces of hydrophobic leaves modified by pathogens at different growth stages. *ACS Nano* **16**, 1318 (2022).
18. Li, Z. et al. Droplet splash and spread on superhydrophobic lotus leaves: direct regulation by tuning the chain length of surfactant. *Colloid. Surface. A* **648**, 129178 (2022).
19. Tang, J. et al. Deposition and water repelling of temperature-responsive nanopesticides on leaves. *Nat. Commun.* **14**, 6401 (2023).
20. Lu, Y. et al. Biomimetic surfaces with anisotropic sliding wetting by energy-modulation femtosecond laser irradiation for enhanced water collection. *RSC Adv.* **7**, 11170 (2017).
21. Karabourniotis, G. et al. The optical properties of leaf structural elements and their contribution to photosynthetic performance and photoprotection. *Plants* **10**, 1455 (2021).
22. Xiang, Y. et al. Controlling pesticide loss through nanonetworks. *ACS Sustain. Chem. Eng.* **2**, 918 (2014).
23. Rana, A. S. et al. Microemulsions as potential pesticidal carriers: a review. *J. Mol. Liq.* **390**, 122969 (2023).
24. Luo, J. et al. Pyraclostrobin loaded lignin-modified nanocapsules: delivery efficiency enhancement in soil improved control efficacy on tomato Fusarium crown and root rot. *Chem. Eng. J.* **394**, 124854 (2020).
25. Chen, G. et al. Chitooligosaccharide modified pesticide-loaded polyurethane microcapsules to mitigate drought stress in wheat. *Chem. Eng. J.* **479**, 147688 (2024).
26. Rao, J. et al. Preparation of microcapsule suspension of herbicide oxyfluorfen polyurea and its effects on phytotoxicity on rice crop. *J. Dispers. Sci. Technol.* **44**, 475 (2021).
27. Wu, T. et al. Eco-friendly water-based λ-cyhalothrin polydopamine microcapsule suspension with high adhesion on leaf for reducing pesticides loss. *J. Agric. Food Chem.* **68**, 12549 (2020).

28. Yin, F. et al. Microemulsion preparation of Waltheria indica extracts and preliminary antifungal mechanism exploration. *Ind. Crop Prod.* **172**, 114000 (2021).
29. Sun, C. et al. Encapsulation and controlled release of hydrophilic pesticide in shell cross-linked nanocapsules containing aqueous core. *Int. J. Pharm.* **463**, 108 (2014).
30. Sheng, W. et al. A facile route to fabricate a biodegradable hydrogel for controlled pesticide release. *RSC Adv.* **5**, 13867 (2015).
31. Adams, E. et al. Co-formulants and adjuvants affect the acute aquatic and terrestrial toxicity of a cycloxydim herbicide formulation to European common frogs (Rana temporaria). *Sci. Total Environ.* **789**, 147865 (2021).
32. Mina, I. R. et al. The critical role of biofilms in bacterial vascular plant pathogenesis. *Plant Pathol.* **68**, 1439 (2019).
33. Das, A., & Ghosh, S. et al. Stimuli-responsive self-assembly of a naphthalene diimide by orthogonal hydrogen bonding and its coassembly with a pyrene derivative by a pseudo-intramolecular charge-transfer interaction. *Angew. Chem. Int. Edit.* **53**, 1092 (2013).
34. Li, X. et al. Supramolecular antibacterial materials for combatting antibiotic resistance. *Adv. Mater.* **31**, 1805092 (2018).
35. Chang, Y. et al. Molecular engineering of polymeric supramphiphiles. *Chem. Soc. Rev.* **48**, 989 (2019).
36. Bai, H. et al. Supramolecular germicide switches through host-guest interactions for decelerating emergence of drug-resistant pathogens. *ChemistrySelect* **2**, 7940 (2017).
37. Gao, C. et al. A user-friendly herbicide derived from photo-responsive supramolecular vesicles. *Nat. Commun.* **9**, 2967 (2018).
38. Zhou, Y. et al. Supramolecular-macrocycle-based crystalline organic materials. *Adv. Mater.* **32**, 1904828 (2019).
39. Yu, G. & Chen, X. Host-guest chemistry in supramolecular theranostics. *Theranostics* **9**, 3041 (2019).
40. Chen, Y. et al. Controllable macrocyclic supramolecular assemblies in aqueous solution. *Sci. China Chem.* **61**, 979 (2018).
41. Chen, Y. et al. Cytotoxicity regulated by host–guest interactions: a supramolecular strategy to realize controlled disguise and exposure. *ACS Appl. Mater. Interfaces* **8**, 22780 (2016).
42. Yin, H. et al. Recent advances in supramolecular antidotes. *Theranostics* **11**, 1513 (2021).
43. Zhan, W. et al. Fabrication of supramolecular bioactive surfaces via *β*-cyclodextrin-based host–guest interactions. *ACS Appl. Mater. Interfaces* **10**, 36585 (2018).
44. Celebioglu, A., Yildiz, Z. I. & Uyar, T. Thymol/cyclodextrin inclusion complex nanofibrous webs: enhanced water solubility, high thermal stability and antioxidant property of thymol. *Food Res. Int.* **106**, 280 (2018).
45. Zhou, C. et al. Tuning antibacterial activity of cyclodextrin-attached cationic ammonium surfactants by a supramolecular approach. *ACS Appl. Mater. Interfaces* **9**, 31657 (2017).
46. Zhang, J. & Ma, P. X. Cyclodextrin-based supramolecular systems for drug delivery: recent progress and future perspective. *Adv. Drug Deliv. Rev.* **65**, 1215 (2013).
47. Lee, W. et al. Photooxidation driven formation of Fe-Au linked ferrocene-based single-molecule junctions. *Nat. Commun.* **15**, 1439 (2024).
48. Das, S. et al. Novel ferrocene-pyrazolo[1,5-a]pyrimidine hybrids: a facile environment-friendly regioselective synthesis, structure elucidation, and their antioxidant, antibacterial, and anti-biofilm activities. *J. Chem. Sci.* **134**, 79 (2022).
49. Arumugam, N. et al. Synthesis, X-ray structural determination and biological evaluation of novel ferrocene grafted spiroquinoxalinopyrrolidine. *J. Mol. Struct.* **1226**, 129348 (2021).
50. Singh, A. et al. Synthesis and preliminary antimicrobial analysis of isatin–ferrocene and isatin–ferrocenyl chalcone conjugates. *ACS Omega* **3**, 5808 (2018).
51. Ludwig, B. S., Correia, J. D. & Kühn, F. E. Ferrocene derivatives as anti-infective agents. *Coordin. Chem. Rev.* **396**, 22 (2019).
52. Quintana, C. et al. Cyrhetrenyl and ferrocenyl 1,3,4-thiadiazole derivatives: Synthesis, characterization, crystal structures and in vitro antitubercular activity. *Inorg. Chem. Commun.* **55**, 48 (2015).
53. Cheng, Q. et al. Design of ferrocenylseleno-dopamine derivatives to optimize the Fenton-like reaction efficiency and antitumor efficacy. *RSC Adv.* **11**, 25477 (2021).
54. Wong, Y. K. et al. Artemisinin as an anticancer drug: Recent advances in target profiling and mechanisms of action. *Med. Res. Rev.* **37**, 1492 (2017).
55. Realista, S. et al. Electrochemical studies and potential anticancer activity in ferrocene derivatives. *J. Coord. Chem.* **70**, 314 (2016).
56. Xi, G. L. & Liu, Z. Q. Solvent-free Povarov reaction for synthesizing ferrocenyl quinolines: antioxidant abilities deriving from ferrocene moiety. *Eur. J. Med. Chem.* **86**, 759 (2014).
57. Zhang, J. J. et al. Resistance-driven innovations in the discovery of bactericides: novel triclosan derivatives decorating isopropanolamine moiety as promising anti-biofilm agents against destructive plant bacterial diseases. *Pest Manag. Sci.* **79**, 2443 (2023).
58. Zhang, Z. J. et al. Discovery of *β*-carboline oxadiazole derivatives as fungicidal agents against rice sheath blight. *J. Agric. Food Chem.* **66**, 9598 (2018).
59. Yuan, Z. et al. Redox-controlled voltage responsive micelles assembled by noncovalently grafted polymers for controlled drug release. *Macromolecules* **52**, 1400 (2019).
60. Kasprzak, A. et al. Supramolecular interactions between *β*-cyclodextrin and the nucleobase derivatives of ferrocene. *J. Org. Chem.* **84**, 15900 (2019).
61. Chun, F. et al. Self-assembly of amphiphilic homopolymers bearing ferrocene and carboxyl functionalities: effect of polymer concentration, *β*-cyclodextrin, and length of alkyl linker. *Langmuir* **29**, 10922 (2013).
62. Zhang, E. et al. A highly efficient bionic self-healing flexible waterborne polyurethane elastic film based on a cyclodextrin–ferrocene host–guest interaction. *Polym. Chem.* **12**, 831 (2021).
63. Zhang, W., Chen, M. & Diao, G. Preparation and electrochemical behavior of water-soluble inclusion complex of ferrocene with *β*-cyclodextrin polymer. *Electrochim. Acta* **56**, 5129 (2011).
64. Köhler, H. R. & Triebskorn, R. Wildlife ecotoxicology of pesticides: can we track effects to the population level and beyond? *Science* **341**, 759 (2013).
65. Butler Ellis, M. C., Webb, D. A. & Western, N. M. The effect of different spray liquids on the foliar retention of agricultural sprays by wheat plants in a canopy. *Pest Manag. Sci.* **60**, 786 (2004).
66. Gao, Y. et al. Wetting and adhesion behavior on apple tree leaf surface by adding different surfactants. *Colloid. Surface. B* **187**, 110602 (2020).
67. Zhao, K. et al. Topology-regulated pesticide retention on plant leaves through concave janus carriers. *ACS Sustain. Chem. Eng.* **7**, 13148 (2019).
68. Zhao, M. et al. pH/redox dual responsive from natural polymer-based nanoparticles for on-demand delivery of pesticides. *Chem. Eng. J.* **435**, 134861 (2022).
69. Singh, A. et al. Anti-biofilm and anti-virulence potential of 3,7-dimethyloct-6-enal derived from Citrus hystrix against bacterial blight of rice caused by *Xanthomonas oryzae* pv. *oryzae*. *Microb. Pathog.* **115**, 264 (2018).
70. Liang, W. et al. pH-responsive on-demand alkaloids release from core–shell ZnO@ZIF-8 nanosphere for synergistic control of bacterial wilt disease. *ACS Nano* **16**, 2762 (2022).
71. Huang, X. et al. Rational optimization of 1, 2, 3-triazole-tailored carbazoles as prospective antibacterial alternatives with significant

in vivo control efficiency and unique mode of action. *J. Agric. Food Chem.* **69**, 4615–4627 (2021).
72. Liao, S. et al. Antibacterial activity and mechanism of silver nanoparticles against multidrug-resistant *Pseudomonas aeruginosa*. *Int. J. Nanomed.* **14**, 1469–1487 (2019).
73. Bechtel, W. & Bauer, G. Catalase protects tumor cells from apoptosis induction by intercellular ROS signaling. *Anticancer Res.* **29**, 4541–4557 (2009).
74. Wang, J. et al. The global strategy employed by *Xanthomonas oryzae* pv. *oryzae* to conquer low-oxygen tension. *J. Proteomics* **161**, 68 (2017).
75. Yu, X. et al. Bismerthiazol Inhibits *Xanthomonas citri* subsp. *citri* growth and induces differential expression of citrus defense-related genes. *Phytopathology* **106**, 693 (2016).
76. Liang, X. et al. Two thiadiazole compounds promote rice defence against *Xanthomonas oryzae* pv. *oryzae* by suppressing the bacterium's production of extracellular polysaccharides. *Mol. Plant Pathol.* **16**, 882 (2015).
77. Xie, T. et al. Antibacterial activity of food-grade chitosan against Vibrio parahaemolyticus biofilms. *Microb. Pathog.* **110**, 291–297 (2017).
78. Papaianni, M. et al. Plant Dynamic Metabolic Response to Bacteriophage Treatment After *Xanthomonas campestris* pv. *campestris* Infection. *Front. Microbiol.* **11**, 732 (2020).
79. Liu, J. et al. In-Group" communication in marine vibrio: a review of N-Acyl homoserine lactones-driven quorum sensing. *Front. Cell. Infect. Mi.* **8**, 139 (2018).
80. Mark, F. et al. Thiazolidinedione-8 alters symbiotic relationship in C. albicans-S. mutans dual species biofilm. *Front. Microbiol.* **7**, 140 (2016).
81. Srilatha, M., Patyal, N. & Saddala, M. S. Functional analysis and screening small molecules to RpfF protein in *Xanthomonas oryzae* involved in rice bacterial blight disease. *J. Integr. Agric.* **19**, 735 (2020).
82. Singh, R. P. Attenuation of quorum sensing-mediated virulence in Gram-negative pathogenic bacteria: implications for the post-antibiotic era. *Med. Chem. Commun.* **6**, 259 (2015).
83. Jeong, K. S. et al. Virulence reduction and differing regulation of virulence genes in rpf mutants of *Xanthomonas oryzae* pv. *oryzae*. *Plant Pathol. J.* **24**, 143 (2008).
84. Li, P. et al. Design, synthesis, and evaluation of new sulfone derivatives containing a 1,3,4-oxadiazole moiety as active antibacterial agents. *J. Agric. Food Chem.* **66**, 3093 (2018).
85. Wu, R. et al. Synthesis, antibacterial activity, and action mechanism of novel sulfonamides containing oxyacetal and pyrimidine. *J. Agric. Food Chem.* **70**, 9305 (2022).
86. Zhou, X. et al. Discovery of simple diacylhydrazine-functionalized cinnamic acid derivatives as potential microtubule stabilizers. *Int. J. Mol. Sci.* **23**, 12365 (2022).
87. Gupta, H. R. et al. Embryonic zebrafish model-a well-established method for rapidly assessing the toxicity of homeopathic drugs-toxicity evaluation of homeopathic drugs using zebrafish embryo model. *J. Pharmacopunct.* **19**, 319 (2016).
88. Baran, A. et al. Determination of developmental toxicity of zebrafish exposed to propyl gallate dosed lower than ADI (Acceptable Daily Intake). *Regul. Toxicol. Pharm.* **94**, 16 (2018).
89. Zhang, Y. et al. Scarless wound healing programmed by core-shell microneedles. *Nat. Commun.* **14**, 3431 (2023).
90. Mu, S. et al. Cationic polysaccharide conjugates as antibiotic adjuvants resensitize multidrug-resistant bacteria and prevent resistance. *Adv. Mater.* **34**, 2204065 (2022).
91. Li, H. et al. Sedimentary DNA reveals the link between microbial community dynamics and climate during the late last glaciation in the offshore region of the Zambezi River, Southwest Indian Ocean. *Sci. Total Environ.* **906**, 167787 (2024).

Acknowledgements

We gratefully acknowledge the support from the National Key Research and Development Program (2022YFD1700300), Program for Introducing Talents of Discipline to Universities in China (111 Program, D20023), Central Government's Fund for Local Science and Technology Development (Qiankehezhongyindi (2023) 001), Research and Innovation Team of Guizhou University (Guidakechuangtuan[2023]03), Guizhou Provincial S&T Project (ZK[2022]017), Innovation Program for High-level Talents of Guizhou Province (No. GCC[2023]008), and Natural-Science-Special-Project of Guizhou University (Guidazhuanjihe [2024]02).

Author contributions

J.Y. and K.L. contributed equally to this work. P.W. conceived and designed the study. J.Y., Y.C., and H.Y. performed the experiments. J.Y., K.L., and Y.C. analyzed the data. P.W. checked the data. J.Y. and K.L. wrote the original draft. G.H., F.D., and P.W. reviewed and edited the manuscript. All authors read and approved the final manuscript.

Competing interests

The authors declare no competing interests.

Additional information

Supplementary information The online version contains supplementary material available at https://doi.org/10.1038/s41467-025-57839-x.

Correspondence and requests for materials should be addressed to Fengpei Du or Peiyi Wang.

Peer review information *Nature Communications* thanks Jian-Chun Qin and the other, anonymous, reviewer for their contribution to the peer review of this work. A peer review file is available.